J. Fluid Mech. (2007), *vol.* 592, *pp.* 263–293. © 2007 Cambridge University Press
doi:10.1017/S0022112007008518 Printed in the United Kingdom

Turbulence structure in rough- and smooth-wall boundary layers

R. J. VOLINO[1], M. P. SCHULTZ[2] AND K. A. FLACK[1]

[1]Mechanical Engineering Department, United States Naval Academy, Annapolis, MD 21402, USA

[2]Naval Architecture and Ocean Engineering Department, United States Naval Academy, Annapolis, MD 21402, USA

(Received 9 April 2007 and in revised form 18 July 2007)

Turbulence measurements for rough-wall boundary layers are presented and compared to those for a smooth wall. The rough-wall experiments were made on a woven mesh surface at Reynolds numbers approximately equal to those for the smooth wall. Fully rough conditions were achieved. The present work focuses on turbulence structure, as documented through spectra of the fluctuating velocity components, swirl strength, and two-point auto- and cross-correlations of the fluctuating velocity and swirl. The present results are in good agreement, both qualitatively and quantitatively, with the turbulence structure for smooth-wall boundary layers documented in the literature. The boundary layer is characterized by packets of hairpin vortices which induce low-speed regions with regular spanwise spacing. The same types of structure are observed for the rough- and smooth-wall flows. When the measured quantities are normalized using outer variables, some differences are observed, but quantitative similarity, in large part, holds. The present results support and help to explain the previously documented outer-region similarity in turbulence statistics between smooth- and rough-wall boundary layers.

1. Introduction

The importance of surface roughness is well known for boundary-layer flows. Roughness promotes transition to turbulence in laminar boundary layers. Pressure forces on the roughness elements increase drag when the boundary layer is turbulent. The flow over the top of the roughness elements may experience lower shear than the flow over a solid smooth surface. The pressure forces typically dominate, resulting in increased drag over rough surfaces, but the reduced shear can lower overall drag in some cases (e.g. riblets). In either case, roughness clearly alters the near-wall flow structure. The near-wall streaks documented by Kline *et al.* (1967) in smooth-wall boundary layers, for example, typically have a spacing of about 100 wall units and extend from the wall about the same distance. Roughness elements of this size or larger will undoubtedly disrupt the streaks. The effect of roughness on the outer part of the boundary layer is less obvious. To the extent that roughness-induced turbulent events extend far from the wall, the turbulent structure of the entire boundary layer may be affected. In contrast, if the events induced by the roughness are localized near the wall, the roughness may change the boundary condition for the outer flow but leave its structure qualitatively unchanged. In the latter case, the outer flow structure would be similar for smooth- and rough-wall cases, with the roughness effect appearing through the wall shear, on which the outer flow would scale.

https://doi.org/10.1017/S0022112007008518 Published online by Cambridge University Press

Prediction of roughness effects is of clear practical importance for a wide range of industrial and geophysical flows. Examples range from flow through pipes and over vehicles to atmospheric boundary layers. In principle, rough-wall boundary layers can be predicted through direct numerical simulation of the Navier–Stokes equations if the roughness is accurately incorporated in the boundary conditions. This approach is not practical in most applications, however, so turbulence modelling is required. Turbulence modelling requires prediction of the Reynolds stresses, which in turn must depend on the turbulent eddy structure. Much is already known about the structure of smooth-wall boundary layers, although more remains to be done to link this knowledge to prediction of the Reynolds stresses. To the extent that rough- and smooth-wall boundary layers are similar, the understanding of smooth-wall flows may facilitate prediction of rough-wall boundary layers. The study of the outer region structure in rough-wall cases may help elucidate the relationship between the inner and outer regions of the boundary layer, improving predictions in both rough- and smooth-wall cases.

Much is known concerning the structure of smooth-wall boundary layers. Theodorson (1952) and Townsend (1976) proposed a boundary layer consisting of hairpin vortices rising from the wall. Head & Bandyopadhyay (1981) reported direct observations of hairpins and proposed that hairpins occur in groups with characteristic inclination angles. Antonia, Bisset & Browne (1990) discussed large 'δ-scale' u-discontinuities in the outer layer. Na, Hanratty & Liu (2001) described 'superbursts' of fluid ejected from the near-wall region. Adrian, Meinhart & Tomkins (2000*b*) presented experimental evidence and an extended discussion of hairpin packets. The packets consist of multiple layers of nested hairpin vortices. Perry & Chong (1982) further developed Townsend's (1976) model, proposing 'attached eddies' extending from the wall. Perry & Marušić (1995) extended the model to include both attached and detached eddies. The detached eddies consist of hairpins that have separated from the wall and are responsible for the outer flow structure. Recent discussion of turbulence structure is provided by several others, including but not limited to Adrian, Christensen & Liu (2000*a*), Christensen & Adrian (2001), Marušić (2001), Tomkins & Adrian (2003), Hambleton, Hutchins & Marušić (2006) and Ganapathisubramani, Longmire & Marušić (2006). Many others have presented turbulence statistics, which result from the flow structure. The various views of the turbulent boundary layer are largely compatible. Ganapathisubramani, Longmire & Marušić (2003), for example, noted that superbursts can occur within hairpin packets. Hutchins, Hambleton & Marušić (2005) observed that superbursts, hairpin packets and the large-scale passive wakes of del Álamo & Jiménez (2003) all scale with the boundary-layer thickness, δ.

Perry & Marušić's (1995) description of detached eddies suggests a decoupling of the outer region of the boundary layer from the near wall. Experimental evidence suggests the division between the inner and outer regions occurs at roughly $y/\delta = 0.15$, where y is the distance from the wall. The detached eddies are not directly tied to the wall, so their size should depend on an outer-region scale, i.e. the boundary-layer thickness. The near-wall flow still sets the boundary condition for the outer flow, so the outer region should depend on the wall shear and scale with the friction velocity, u_τ. The wall shear, in turn, depends on the velocity gradient, which is influenced by the outer flow. Hence the decoupling of the inner and outer regions is only partial. Near-wall turbulent events may not directly affect the outer-flow structure, but there is a scaling link through u_τ. The importance of large-scale events in the outer region is significant. Adrian *et al.* (2000*b*) noted the effect of both inner and outer scales on

https://doi.org/10.1017/S0022112007008518 Published online by Cambridge University Press

the spacing of bursts and streaks in the inner region and the height of hairpins in the outer region. Ganapathisubramani *et al.* (2003) noted that hairpin packets contribute a large fraction of the total stress in the boundary layer. Tomkins & Adrian (2003) indicate that both large- and small-scale motions contribute to stresses in the near-wall region. Guala, Hommema & Adrian (2006) found that large and very large flow structures contribute about 80 % of the Reynolds stress in all parts of the boundary layer.

With a few exceptions, most rough-wall studies have inferred turbulence structure through statistics such as the time-averaged Reynolds stresses and higher-order moments. The prospect of structural similarity between rough- and smooth-wall boundary layers is promising, based on numerous experiments that have shown similarity of mean flow and turbulence quantities. The wall similarity hypothesis, which is an extension of Townsend's (1976) concept of Reynolds-number similarity for turbulent flows, states that at high Reynolds number, turbulent motions are independent of wall roughness and viscosity outside the roughness sublayer. The roughness sublayer is defined as the region directly above the roughness where the turbulent motions are directly influenced by the roughness length scales. Similarity outside the roughness sublayer is consistent with Perry & Marušić's (1995) model of detached eddies. An extensive literature review of rough-wall boundary layers by Raupach, Antonia & Rajagopalan (1991) concluded that there is strong experimental evidence of outer-layer similarity in the turbulence structure over smooth and rough walls. However, the experimental studies of rough-wall boundary layers by Krogstad, Antonia & Browne (1992), Tachie, Bergstrom & Balachandar (2000) and Keirsbulck *et al.* (2002) have all observed significant changes to the Reynolds stresses that extend well into the outer layer for flows over woven mesh and transverse bar roughness. Additionally, the numerical simulations of turbulent channel flow by Leonardi *et al.* (2003) and Bhaganagar, Kim & Coleman (2004) show roughness effects in the outer layer. This is in contrast to experimental studies by Flack, Schultz & Shapiro (2005), Kunkel & Marušić (2006), Shockling, Allen & Smits (2006), and Schultz & Flack (2007) which provide support for similarity in smooth- and rough-wall boundary layers in terms of both the mean flow and the Reynolds stresses. Jiménez (2004) states that the conflicting views regarding the validity of the wall similarity hypothesis may be due to the effect of the relative roughness, k/δ, on the flow. He found that the studies that have shown outer-layer effects have been for cases where the roughness height is large compared to the boundary-layer thickness ($k/\delta \geqslant 1/50$). Flack, Schultz & Connelly (2007), however, showed outer-layer similarity even with $k/\delta \geqslant 1/20$ for sandgrain and mesh surfaces.

More direct information obtained through simultaneous measurements at multiple locations or time-resolved measurements may help to clarify the extent of similarity in rough-wall boundary layers. Grass (1971) observed ejections from the near-wall region that extended into the outer layer. These were said to dominate the momentum transport and provide a structural connection between the inner and outer layers. They were a common feature of all boundary layers, however, irrespective of roughness. In the smooth-wall case, the viscous sublayer was the source of the ejected fluid. In the rough-wall case, the ejections originated in the spaces between roughness elements. Turbulence intensity data depended only on the distance from the wall and the boundary shear, and was independent of roughness. Nakagawa & Hanratty (2001) considered flow over a wavy wall and present two-point correlations of the streamwise and wall normal velocity fluctuations. They found good quantitative agreement with similar flows over smooth walls. Jiménez (2004) reported similarity between turbulence

https://doi.org/10.1017/S0022112007008518 Published online by Cambridge University Press

spectra acquired in rough- and smooth-wall boundary layers outside of $y/\delta = 0.15$. Krogstad & Antonia (1994) in contrast, documented the flow over a k-type rough wall and noted significant differences from a smooth wall. The present study considers the structure of smooth- and rough-wall boundary layers though documentation of spectra, swirl strength and two-point correlations.

2. Experiments and data processing

Experiments were conducted in a water tunnel designed for detailed boundary-layer measurements. The test section was 2 m long, 0.2 m wide and nominally 0.1 m high. The lower wall was a flat plate which served as the test wall. The upper wall was adjustable and set for a zero streamwise pressure gradient with the free-stream velocity set to 1.25 m s^{-1} for all cases. The acceleration parameter, defined as

$$K = \frac{\nu}{U_e^2}\frac{\mathrm{d}U_e}{\mathrm{d}x}, \tag{2.1}$$

was less than 5×10^{-9}. The upper wall and sidewalls provided optical access. An acrylic test plate was used for the smooth-wall cases. A woven wire mesh was affixed to a similar plate for the rough-wall cases. The mesh spacing was $t = 1.69$ mm, and the mesh wire diameter was 0.26 mm, resulting in a peak to trough roughness height of $k = 0.52$ mm. Both the smooth and rough plates were painted black to facilitate optical measurements. The smooth plate was sanded after painting to ensure hydrodynamically smooth conditions. The boundary layer was tripped near the leading edge with a 0.8 mm diameter wire, ensuring a turbulent boundary layer. Velocity measurements showed that a core flow remained to the downstream end of the test section.

Flow was supplied to the test section from a 1900 l cylindrical tank. Water was drawn from the tank to two variable-speed pumps operating in parallel and then sent to a flow-conditioning section consisting of a diffuser containing perforated plates, a honeycomb, three screens and a three-dimensional contraction. The test section followed the contraction. The free-stream turbulence level was less than 0.5 %. Water exited the test section through a perforated plate emptying into the cylindrical tank. The test fluid was deionized, filtered and deaerated water. A chiller was used to keep the water temperature constant to within 1 K during all tests.

Boundary-layer velocity measurements were obtained with a TSI FSA3500 two-component laser-Doppler velocimeter (LDV). The LDV consists of a four-beam fibre optic probe that collects data in backscatter mode. A custom-designed beam displacer was added to the probe to shift one of the four beams, resulting in three co-planar beams that can be aligned parallel to the wall. Additionally, a 2.6:1 beam expander was located at the exit of the probe to reduce the size of the measurement volume. The resulting probe volume diameter (d) was 45 μm with a probe volume length (l) of 340 μm. The corresponding measurement volume diameter and length in viscous length scales were $d^+ = 2.3$ and $l^+ = 17.1$ for the smooth-wall case and $d^+ = 3.1$ and $l^+ = 24.5$ for the rough-wall case.

Velocity profiles were acquired at several streamwise stations to determine the boundary-layer thickness. A smooth-wall and a rough-wall station with similar momentum-thickness Reynolds numbers were then selected for further analysis. At each station, the probe was traversed to approximately 40 locations within the boundary layer with a Velmex three-axis traverse unit. The traverse allowed the position of the probe to be maintained to ±5 μm in all directions. The wall normal

https://doi.org/10.1017/S0022112007008518 Published online by Cambridge University Press

velocity component was not obtained for the 8–10 data points closest to the wall owing to very low data rates and wall reflections. A total of 40 000 random velocity samples were obtained at each location in the boundary layer. The data were collected in coincidence mode. The flow was seeded with 3 μm diameter alumina particles. The seed volume was controlled to achieve acceptable data rates while maintaining a low burst density signal (Adrian 1983).

The LDV was also used to acquire long-time records (500 000 readings) at $y/\delta = 0.1$ and 0.4. The flow was seeded with 1 μm diameter alumina particles. While larger particles were acceptable for the other LDV measurements, smaller particles aided in providing sufficient seed particles for the high data rate needed for spectral processing, while maintaining low enough seed volume for an acceptably low burst density. For turbulent spectra, it is important that the measurement volume be small enough so that subsequent particles can be attributable to the same eddy structure. As the results below will show, the correlation coefficients between points spaced $l = 340\,\mu$m in the spanwise direction are typically above 0.95, indicating that the probe volume is sufficiently small to resolve most turbulent structures. The LDV was operated in coincidence mode, and the nominal sampling rate was about 2200 Hz. Data were acquired as particles passed through the measurement volume, so the samples were not evenly spaced in time. Interpolation, using the method of Wei & Willmarth (1989) was used to produce a time trace with evenly spaced points for spectral analysis. To use this method accurately, the nominal sampling rate must be fast enough to provide an essentially continuous signal. This requires very low turbulence energy above the Nyquist frequency. Spectra of the data show that the highest frequency of significant energy containing fluctuations in the flow was less than half the nominal sampling rate.

Flow-field measurements were acquired using particle image velocimetry (PIV). Streamwise–wall normal (x, y) planes were acquired at the spanwise centreline of the test section. Streamwise–spanwise (x, z) planes were acquired at $y/\delta = 0.1$ and 0.4. The flow was seeded with 3 μm diameter alumina particles. The light source was a Nd:YAG laser set for a 300 μs interval between pulses for each image pair. The field of view in the (x, y)-plane was 72 mm × 53 mm, extending from near the wall into the free stream. In the (x, z)-plane the field of view was 71 mm × 53 mm, centred about the midspan of the test section. A CCD camera with a 1376 × 1024 pixel array was used. TSI Insight 6.0 software was used for image processing. Velocity vectors were obtained using 16 or 32 pixel square windows with 50 % overlap. For each measurement plane, 2000 image pairs were acquired for processing.

The data-processing techniques used to compute the mean velocity, turbulence statistics and wall shear are described in detail in Schultz & Flack (2007). The techniques used to compute spectra, spatial correlations and swirl strength are described below.

Spectra and cospectra of the streamwise (u) and wall normal (v) components of the turbulence were computed using 4096 point fast Fourier transforms with 50 % overlap and Hamming windowing. The frequency spectra are converted to wavenumber spectra using Taylor's hypothesis of frozen turbulence. The mean velocity at the measurement location, as opposed to the instantaneous velocity of each data point is used in the conversion. The same technique was used by Guala *et al.* (2006). The frozen turbulence approximation gives a conservative estimate of the wavenumber spectra compared to two-point measurements because large-scale eddies may decay as they convect past the measurement volume. This approximation could potentially affect either the smooth- or rough-wall case more if the decay were stronger in one

https://doi.org/10.1017/S0022112007008518 Published online by Cambridge University Press

case than the other, but as will be shown below, the rough- and smooth-wall spectra were similar.

Two-point spatial correlations were done for each measurement plane. In the (x, y)-plane the correlation is defined at the wall normal position y_{ref} as

$$R_{AB}(y_{ref}) = \frac{\overline{A(x, y_{ref})B(x + \Delta x, y_{ref} + \Delta y)}}{\sigma_A(y_{ref})\sigma_B(y_{ref} + \Delta y)}, \tag{2.2}$$

where A and B are the quantities of interest at two locations separated in the streamwise and wall normal directions by Δx and Δy, and σ_A and σ_B are the standard deviations of A and B at y_{ref} and $y_{ref} + \Delta y$, respectively. At every y_{ref}, the overbar indicates the correlations were averaged among locations pairs with the same Δx and Δy, and then time averaged over the 2000 vector fields. Correlations of u, v, the swirl strength, and all cross-correlations were considered.

For the (x, z)-planes, the correlation is defined as

$$R_{AB} = \frac{\overline{A(x, z)B(x + \Delta x, z + \Delta z)}}{\sigma_A\sigma_B}, \tag{2.3}$$

where A and B are the quantities of interest at two locations separated in the streamwise and spanwise directions by Δx and Δz, and σ_A and σ_B are the standard deviations of A and B based on data in the full plane for the 2000 vector fields. The correlations were averaged among all locations with the same Δx and Δz, and then time averaged. The same averaging techniques were used by Tomkins & Adrian (2003) and Ganapathisubramani *et al.* (2005).

The swirl strength, λ, can be used to locate vortices. It is closely related to the vorticity, but discriminates between vorticity due only to shear and vorticity resulting from rotation. It is defined as the imaginary part of the complex eigenvalue of the local velocity gradient tensor, and is defined as follows (Zhou *et al.* 1999):

$$[d_{ij}] = [v_r \quad v_{cr} \quad v_{ci}] \begin{bmatrix} \lambda_r & & \\ & \lambda_{cr} & \lambda_{ci} \\ & -\lambda_{ci} & \lambda_{cr} \end{bmatrix} [v_r \quad v_{cr} \quad v_{ci}]^{-1}, \tag{2.4}$$

where $[d_{ij}]$ is the velocity gradient tensor. It is used in the present study in a two-dimensional form as explained in several studies including Hutchins *et al.* (2005). A more complete discussion is available in Chong, Perry & Cantwell (1990). By definition, λ is always $\geqslant 0$, but a sign can be assigned based on the local vorticity to show the direction of rotation. Swirl strength, λ, will be assumed signed unless denoted λ_m, which will indicate the unsigned magnitude. In the (x, y)-plane, λ can be used to identify the heads of hairpin vortices, and in the (x, z)-plane, λ can identify the legs of these vortices.

3. Results

Comparisons are made between the flow at the smooth-wall location with the highest Reynolds number and the rough-wall location with the closest Reynolds number to the smooth-wall case, with the focus being on turbulence structure. The boundary-layer thickness, friction velocity and other quantities from the velocity profiles at these locations are presented in table 1. For the rough-wall case, the roughness Reynolds number, $k_s^+ = k_s u_\tau/\nu$ (k_s is the equivalent sandgrain roughness), is 112, indicating fully rough conditions. The roughness Reynolds number is given by

https://doi.org/10.1017/S0022112007008518 Published online by Cambridge University Press

Wall	x (m)	U_e (m s^{-1})	δ (mm)	u_τ (m s^{-1})	$Re_\theta = U_e\theta/\nu$	$Re_\tau = u_\tau\delta/\nu$	$k_s^+ = k_s u_\tau/\nu$	k/δ
Smooth	1.50	1.255	35.2	0.0465	6069	1772		
Rough	1.08	1.247	36.8	0.0603	7663	2438	112	0.014

TABLE 1. Boundary-layer parameters.

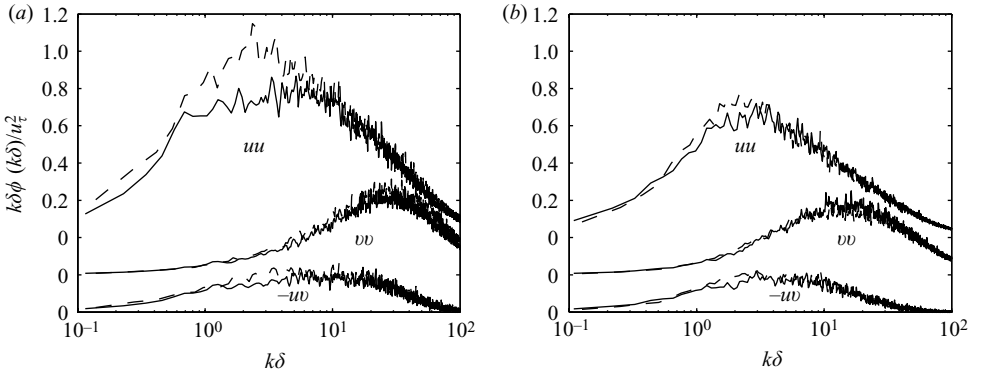


FIGURE 1. Premultiplied turbulence spectra of uu, vv, and $-uv$ at (a) $y/\delta = 0.1$ and (b) $y/\delta = 0.4$. ——, smooth; – – –, rough.

the following (Schultz & Flack 2007)

$$\Delta U^+ = \frac{1}{\kappa} \ln k_s^+ - 3.5, \tag{3.1}$$

where ΔU^+ is the roughness function. The friction velocity, u_τ, was determined using the Clauser chart method with $\kappa = 0.41$ and $B = 5.0$. The uncertainty in u_τ was $\pm 3\,\%$ and $\pm 6\,\%$ for the smooth- and rough-wall cases, respectively. The total stress method was also used to evaluate u_τ, and the resulting values agreed with those from the Clauser chart method to within 5 %. Details of both methods are given in Flack *et al.* (2005). The uncertainties in the boundary-layer thickness (based here on $U/U_e = 0.99$) and momentum thickness were 7 % and 4 %, respectively.

3.1. *Spectra*

Premultiplied spectra of uu, vv and $-uv$ are shown in figure 1, normalized using outer variables. At $y/\delta = 0.1$ (figure 5a), there is a difference between the rough- and smooth-wall uu spectra at low wavenumbers. At higher wavenumbers for uu and for all wavenumbers in vv and uv, the smooth- and rough-wall spectra are similar. The overall difference in uu between the two cases is about 20 %, which is large enough to indicate a possible difference between the cases, but still within the combined uncertainty of the measurements. At $y/\delta = 0.4$, the rough and smooth cases agree to within 3 %. The rough-wall boundary layer contains significantly more turbulent energy than the smooth, but when scaled with u_τ, the similarity between the rough and smooth cases is clear in the outer flow. The present results contrast with those of Krogstad *et al.* (1992). Their results showed significant increases in the vv spectrum over the entire wavenumber range for a rough wall.

https://doi.org/10.1017/S0022112007008518 Published online by Cambridge University Press

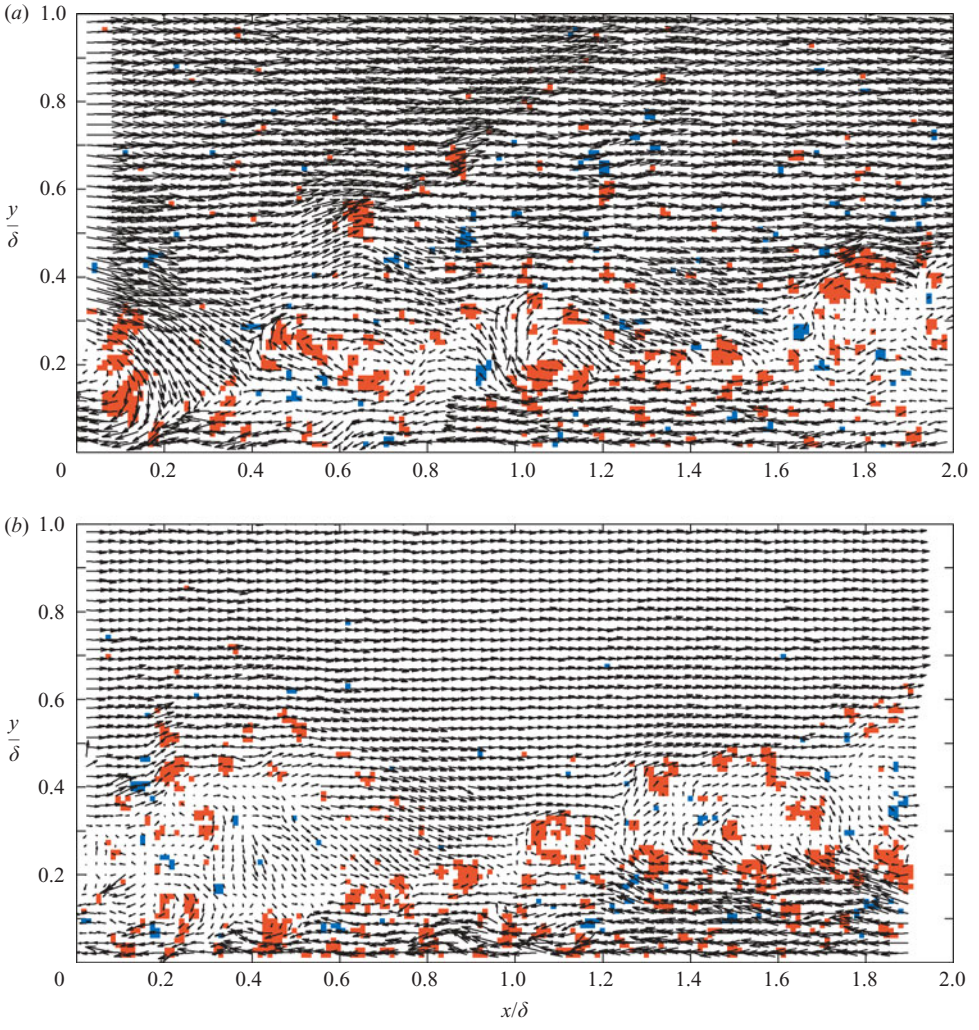


FIGURE 2. Typical instantaneous velocity field in the (x, y)-plane with positive (prograde) swirl (red shading) and negative (retrograde) swirl (blue shading) superimposed, (*a*) smooth wall, (*b*) rough wall.

3.2. *Velocity fields, (x, y)-plane*

Typical instantaneous velocity vector fields in the streamwise–wall normal plane are shown in figure 2. A Galilean decomposition has been applied. That is, a uniform convection velocity ($0.72U_e$ in the smooth-wall case and $0.64U_e$ in the rough-wall case) has been subtracted from each field. The hairpin vortices in a packet become visible if their common convection velocity is subtracted from the instantaneous field. The fields shown in figure 2 were deliberately chosen to include hairpin packets. Qualitatively, the smooth- and rough-wall velocity fields look very similar. Lines of vortices, inclined at about 10° to 15° to the wall, are visible in both cases. These vortices are the heads of hairpins moving together as a packet. Vortices rotating in the direction exhibited by the hairpin heads (clockwise in figure 2) were termed prograde by Wu & Christensen (2006). They referred to vortices rotating in the opposite direction as retrograde. Superimposed on the vectors in figure 2 are contours

https://doi.org/10.1017/S0022112007008518 Published online by Cambridge University Press

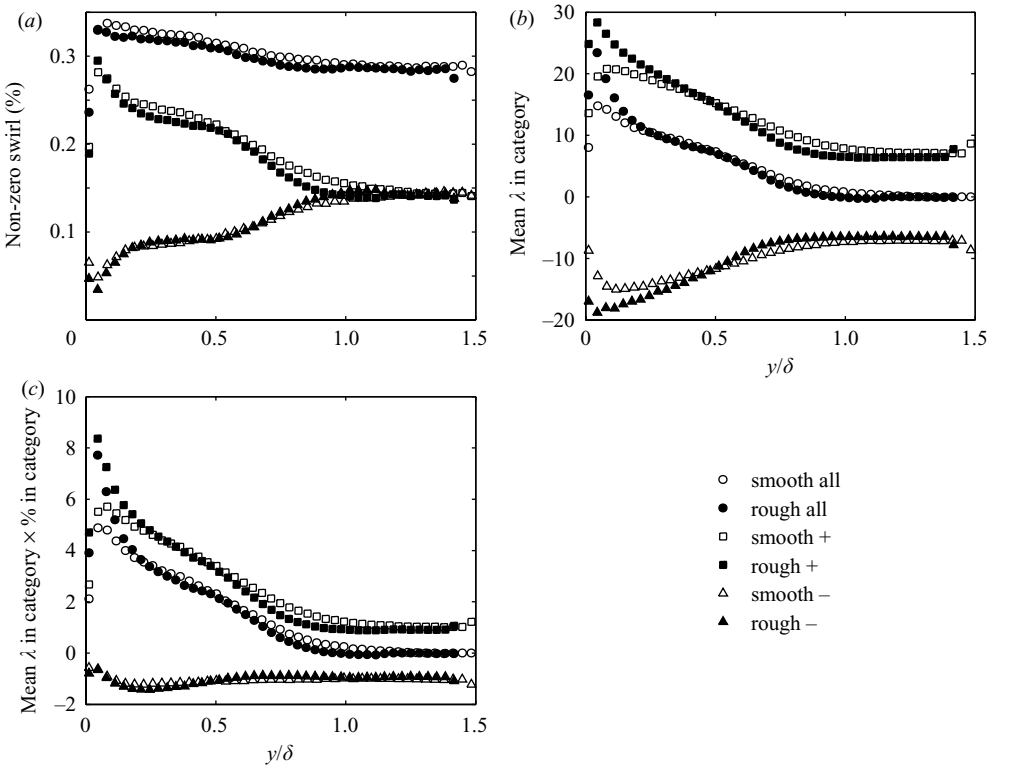


FIGURE 3. Swirl strength in the (x, y)-plane, (a) fraction of time with positive, negative and non-zero swirl strength, (b) average dimensionless swirl strength during positive, negative and non-zero swirl events, (c) product of fraction of time with positive, negative and non-zero swirl strength and corresponding average swirl within fraction.

of signed swirl strength. The regions of non-zero swirl strength are almost always associated with hairpin packets. This is most evident in figure 2(b), in which the end of a mature hairpin packet is seen on the left ($x/\delta < 0.6$) with another hairpin packet extending nearly the entire width of the image ($0 < x/\delta < 1.9$). The hairpin heads visible in the velocity vectors correspond to regions of positive (prograde) λ. These are dominant features of the flow since they are generated by the mean shear. Other regions of positive swirl are also visible, and most of these are attributable to other hairpin packets moving at different convection velocities. These packets become clear when different convection speeds are subtracted from the velocity field. The present results for both rough and smooth walls are in qualitative agreement with the findings of Adrian *et al.* (2000*b*), which showed these packets to be a significant feature of the smooth-wall boundary layer. Below, more quantitative comparisons between the two cases will be made.

The swirl strength is quantified in figure 3. The fraction of measurement locations with positive (prograde) and negative (retrograde) λ are shown as a function of y/δ in figure 3(a). Also shown is the sum of the positive and negative fractions, i.e. the fraction of locations with non-zero swirl. The data in figure 3 are based on all 2000 vector fields for each of the smooth- and rough-wall cases. The agreement between the smooth- and rough-wall cases is very good. At all locations, the swirl strength at any instant is non-zero about 30 % of the time. Near the wall, most of this non-zero swirl

https://doi.org/10.1017/S0022112007008518 Published online by Cambridge University Press

has a positive sense of rotation. This is expected, as the heads of hairpin vortices have positive vorticity. Wu & Christensen (2006) reported the same observation for smooth walls. With increasing distance from the wall, the fraction of positive swirl decreases and the fraction of negative swirl rises at about the same rate. The rate of change of these quantities is rapid from the wall to $y/\delta \approx 0.15$, and then becomes more gradual at y/δ between 0.15 and 0.55. These two regions correspond to the regions it has been proposed are associated with attached and detached eddies. Beyond $y/\delta = 0.55$, the rate of change of the fractions increases, and by the edge of the boundary layer, the positive and negative fractions are equal. The locations near the boundary-layer edge are above most hairpin packets, so the turbulent motions will be less organized and vortices with positive and negative rotation should be equally likely.

The mean of the dimensionless swirl strength, $\overline{\lambda}\delta/\mathrm{u}_\tau$, corresponding to the positive, negative and non-zero fractions of figure 3(*a*) is shown in figure 3(*b*). For $y/\delta < 0.1$, the swirl has noticeably larger magnitude on the rough wall, but for the outer flow the rough- and smooth-wall results are similar. Figure 3(*c*) shows the product of the fractions and mean values of figures 3(*a*) and 3(*b*). The positive swirl contribution is much larger than the negative, and the rough- and smooth-wall results agree well in the outer flow.

The probability density function of λ is presented in figure 4 as a function of y/δ. The value of λ is zero at locations where vortices are not present, which constitutes about 70 % of the flow at any location, as shown in figure 3(*a*). The spikes at zero have been removed from the p.d.f.s of figure 4 for clarity. Near the wall, at $y/\delta = 0.1$ and 0.2, some differences between the rough- and smooth-wall cases are visible. Farther from the wall, at y/δ between 0.4 and 0.6 the smooth- and rough-wall results are nearly indistinguishable, providing more quantitative confirmation of the qualitative agreement observed in figure 2. Near the wall, the positive p.d.f. peak is larger than the negative peak, in agreement with the fractions of figure 3(*a*), since much of the swirl is associated with hairpin heads that have a positive sense of rotation owing to the mean shear. Above $y/\delta = 0.6$, the positive and negative peaks have more equal magnitudes. The $y/\delta > 0.6$ locations are above most of the hairpin packets, so the turbulence is more disorganized with eddies of either sense of rotation.

The shape of both the positive and negative sides of the p.d.f.s in figure 4 are closely approximated by the gamma function probability density function,

$$\gamma = \frac{1}{b^a \Gamma(a)} x^{a-1} \exp(-x/b) \tag{3.2}$$

where a and b are shape and scale parameters. This is demonstrated in figure 5, where the p.d.f. at $y/\delta = 0.4$ is shown along with gamma function fits to the smooth-wall data.

The average extent and shape of the hairpin packets can be quantified through two-point correlations of the fluctuating velocity. Figures 6(*a*) and 6(*b*) show contours of the two-point correlations of the streamwise fluctuating velocity, R_{uu}, with the correlation centred at $y_{ref}/\delta = 0.4$. The rough- and smooth-wall results appear similar. Figure 6(*c*) shows streamwise slices through the correlations of figures 6(*a*) and 6(*b*), passing through the self-correlation peaks. The agreement between the smooth and rough cases is good. Figure 6(*d*) shows wall normal slices passing through the self-correlation peaks. The normalizing quantities in R_{uu} become small near the boundary-layer edge owing to the low free-stream turbulence, resulting in higher uncertainty and more case to case variation. For this reason, only data for $y/\delta < 0.6$ are presented. The rough- and smooth-wall results agree to within 0.06 in R_{uu} from $y/\delta = 0.15$ to

https://doi.org/10.1017/S0022112007008518 Published online by Cambridge University Press

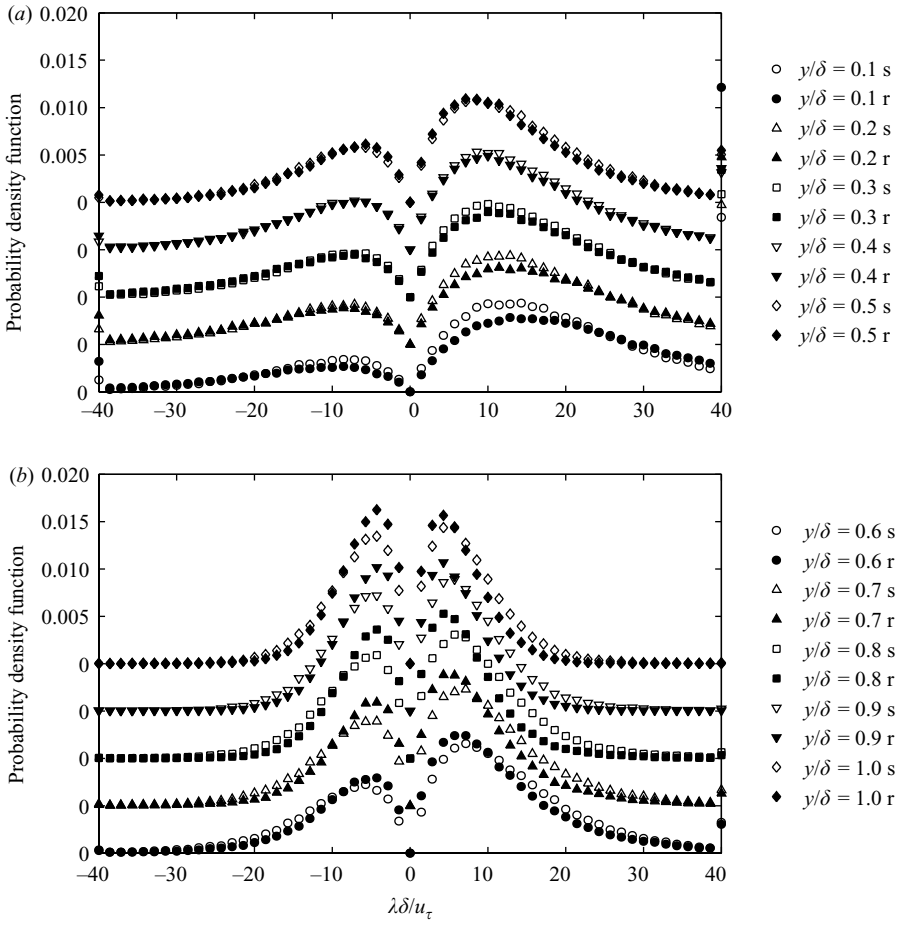


FIGURE 4. Probability density function of signed dimensionless swirl strength in the (x, y)-plane, (a) $y/\delta = 0.1$ to 0.5, (b) $y/\delta = 0.6$ to 1.0.

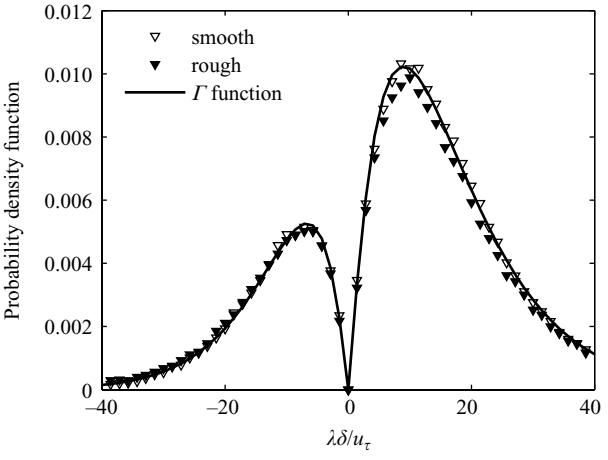


FIGURE 5. Probability density function of signed dimensionless swirl strength in the (x, y)-plane at $y/\delta = 0.4$ with Γ function p.d.f. fit to smooth-wall data.

https://doi.org/10.1017/S0022112007008518 Published online by Cambridge University Press

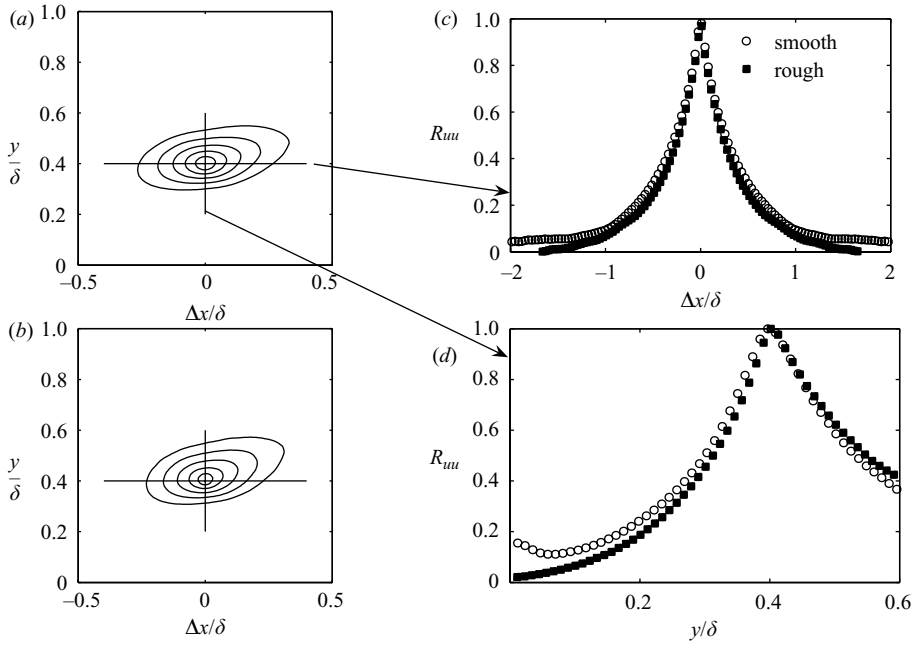


FIGURE 6. Contours of R_{uu} centred at $y/\delta = 0.4$, outermost contour $R_{uu} = 0.5$, contour spacing 0.1, (*a*) smooth wall, (*b*) rough wall, (*c*) streamwise slices through self-correlation points, (*d*) wall normal slices through self-correlation points.

0.6. Nearer to the wall, larger differences are observed. Adrian *et al.* (2000*b*) noted the relation between vortices in hairpin packets, including the interaction between larger, more mature hairpins in the outer flow and smaller vortices associated with the low-speed streaks very near the wall. Although no final conclusion can be drawn because of experimental uncertainty in the near-wall region, the higher R_{uu} at $y/\delta < 0.15$ for the smooth-wall case in figure 6(*d*) may be indicative of this interaction, whereas the lower value for the rough-wall case may result from the destruction of the near-wall streaks by the roughness. Since the outer flow is similar for the rough- and smooth-wall cases, whereas the near-wall flow is different, it seems that the near-wall flow may depend on the outer-flow behaviour, but the outer flow may be independent of the near-wall condition. This would support the wall similarity hypothesis and the detached eddy model for the outer flow.

The angle of inclination of R_{uu} is related to the average inclination of the hairpin packets. Christensen & Wu (2005) determined the angle through a least-squares method by fitting a line through points on the R_{uu} contours. In the present study, a least-squares fit was made to the points farthest away from the self-correlation peak at each of the five contour levels 0.5, 0.6, 0.7, 0.8 and 0.9 both upstream and downstream of the self-correlation peak. For the present cases, the inclination angle remains nearly constant for reference points between $y/\delta = 0.2$ and 0.7. For $y/\delta < 0.2$ there is some scatter in the data as the contours began to merge with the wall. For $y/\delta > 0.7$, the angle decreases toward zero, as these points tend to be above the hairpin packets which produce the inclination. For $0.2 < y/\delta < 0.7$, the angles are $13.2^\circ \pm 2.5^\circ$ and $15.8^\circ \pm 3.3^\circ$ on the smooth and rough walls, respectively. The range in each case indicates the span about the average observed between $y/\delta = 0.2$ and 0.7. The difference between the rough and smooth cases is comparable to the scatter

https://doi.org/10.1017/S0022112007008518 Published online by Cambridge University Press

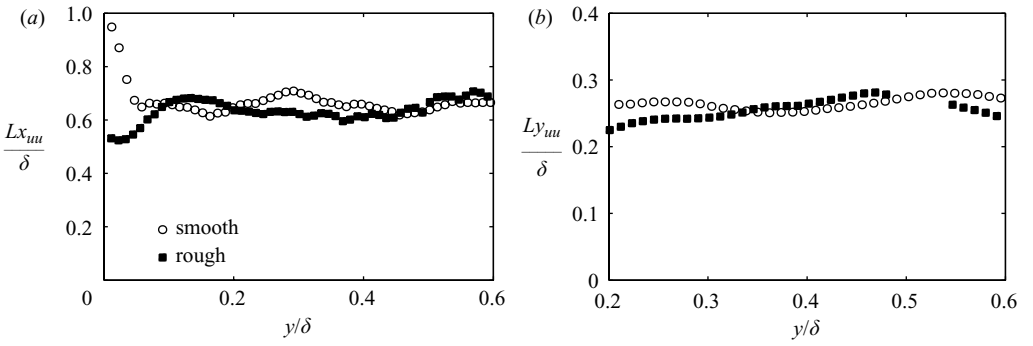


FIGURE 7. Extent of $R_{uu} = 0.5$ contour as function of y/δ, (*a*) streamwise extent, (*b*) wall normal extent.

in the data and the range reported in the literature for smooth-wall boundary layers. Christensen & Wu (2005) found an angle of 11° for their smooth-wall channel flow. Head & Bandyopadhyay (1981) observed inclination angles between 15° and 20°. Christensen & Adrian (2001) reported 12° to 13°. Adrian *et al.* (2000*b*) found a 12° angle. Tomkins & Adrian (2003) found angles between 10° and 20°. Nakagawa & Hanratty (2001) considered a rough (wavy) wall in a channel flow. They found an angle of 9°, which compared to smooth-wall values of 6° to 8°. Krogstad & Antonia (1994), in contrast, saw large differences with roughness. They used mesh roughness, similar to the present study, with $\delta/k = 109$, $\delta/k_s = 15$, $k_s^+ = 331$, and $\delta/t = 24$ at $Re_\theta = 12\,800$. As in the present study, t is the mesh spacing. The Re_θ value is approximately twice that in the present study. Krogstad & Antonia (1994) produced spatial correlations using data acquired with a rake of cross-wire probes at a single streamwise location. Taylor's hypothesis was used to extrapolate in the streamwise direction. Krogstad & Antonia (1994) found an increase in the inclination angle from 10° on a smooth wall to 38° on their rough wall.

The streamwise and wall normal extent of R_{uu} are shown in figure 7. The distance, Lx_{uu}, is defined as in Christensen & Wu (2005) as twice the distance from the self-correlation peak to the most downstream location on the $R_{uu} = 0.5$ contour. The rough- and smooth-wall results agree well with a value of about $Lx_{uu}/\delta = 0.65$ between $y/\delta = 0.1$ and 0.6. Closer to the wall, some differences are visible. If the $R_{uu} = 0.6$ contour is used to determine Lx_{uu}, the results appear qualitatively similar to those in figure 7(*a*), but Lx_{uu}/δ decreases to 0.43 between $y/\delta = 0.1$ and 0.6. This value agrees well with the smooth-wall result of Krogstad & Antonia (1994). In contrast to the present rough- and smooth-wall agreement, Krogstad & Antonia (1994) found Lx_{uu}/δ was about 50 % lower on their rough wall. The wall normal extent of the R_{uu} correlation, Ly_{uu}, is determined based on the wall normal distance between the points closest and farthest from the wall on a particular contour. Figure 7(*b*) shows Ly_{uu}/δ as a function of y/δ using the $R_{uu} = 0.5$ contour. Owing to the contours merging with the wall, reliable estimates of Ly_{uu} could not be obtained for $y/\delta < 0.2$. As with Lx_{uu}, the rough- and smooth-wall results agree well out to $y/\delta = 0.6$. Comparing figures 7(*a*) and 7(*b*), the ratio of Lx_{uu}/Ly_{uu} is roughly 2.5 for both the rough and smooth walls. This is near the range of values reported by Nakagawa & Hanratty (2001) and also agrees with the smooth-wall results of Krogstad & Antonia (1994). In contrast, Krogstad & Antonia (1994) found that the ratio was about 1 on their rough wall.

https://doi.org/10.1017/S0022112007008518 Published online by Cambridge University Press

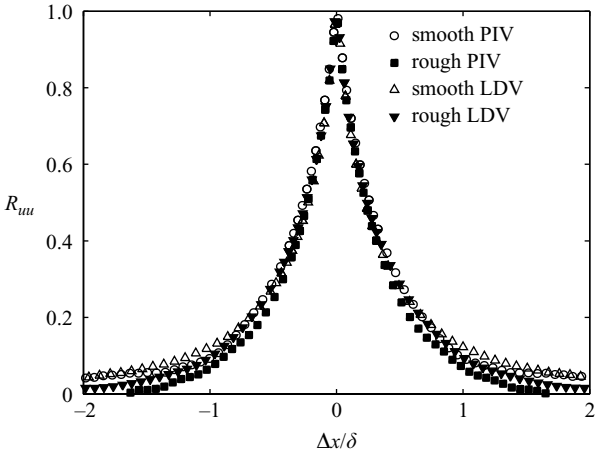


FIGURE 8. Streamwise slices of R_{uu} through the self-correlation point centred at $y/\delta = 0.4$ computed from PIV and LDV data.

The results for the R_{uu} correlation obtained using PIV were compared with the results obtained using LDV at $y/\delta = 0.4$. Determining the R_{uu} correlation based on LDV requires the use of Taylor's hypothesis. The comparison is shown in figure 8. For the rough-wall case, the PIV and LDV results agree to within 10 % for $\Delta x/\delta < 0.4$. For the smooth-wall case, the PIV and LDV results agree to within 10 % for $\Delta x/\delta < 0.8$.

Figure 9 shows R_{vv} contours centred at $y/\delta = 0.4$ along with streamwise and wall normal slices through the self-correlation peaks. Figure 10 shows Lx_{vv} and Ly_{vv} as functions of y/δ. The length Lx_{vv} is determined based on the streamwise distance between the most upstream and downstream points on the $R_{vv} = 0.5$ contour. The length Ly_{vv} is defined as above for the R_{uu} results. The streamwise extent of R_{vv} is considerably less than that of R_{uu}, since R_{uu} is tied to the common convection velocity of each hairpin packet. The ratio Lx_{vv}/Ly_{vv} is about 0.8 for both the smooth and rough walls, which is similar to the results of Nakagawa & Hanratty (2001). The extent of the rough-wall R_{vv} is about 20 % lower than the smooth-wall extent for $y/\delta > 0.2$ in both the streamwise and wall normal directions. The present smooth-wall results are similar to those of Krogstad & Antonia (1994). Krogstad & Antonia (1994) show little difference in Ly_{vv} between their rough- and smooth-wall cases, but Lx_{vv} dropped by a factor of 2 from the smooth wall to the rough.

Contours of the cross-correlation R_{uv} centred at $y/\delta = 0.4$ are shown in figure 11 along with streamwise and wall normal slices through the self-correlation locations. Some differences are present for the lower-magnitude contours, particularly far from the wall, where the rough-wall values are significantly higher. As discussed above, this may be due to free-stream effects and uncertainty in R_{uv} near the boundary-layer edge owing to low turbulence levels. The differences in the higher magnitude contours are consistent with those of R_{vv} in figure 9.

Contours of the auto-correlation of the signed swirl strength, $R_{\lambda\lambda}$, at $y/\delta = 0.4$ are shown in figure 12 along with streamwise and wall normal slices through the self-correlation point. The extent of the $R_{\lambda\lambda} = 0.1$ and 0.2 contours is about 20 % larger for the smooth-wall case. The difference is lower for the higher-valued contours. The streamwise and wall normal extent of the correlation, $Lx_{\lambda\lambda}$ and $Ly_{\lambda\lambda}$, based on the $R_{\lambda\lambda} = 0.5$ contour are shown in figure 13. The extent of the rough-wall correlation is

https://doi.org/10.1017/S0022112007008518 Published online by Cambridge University Press

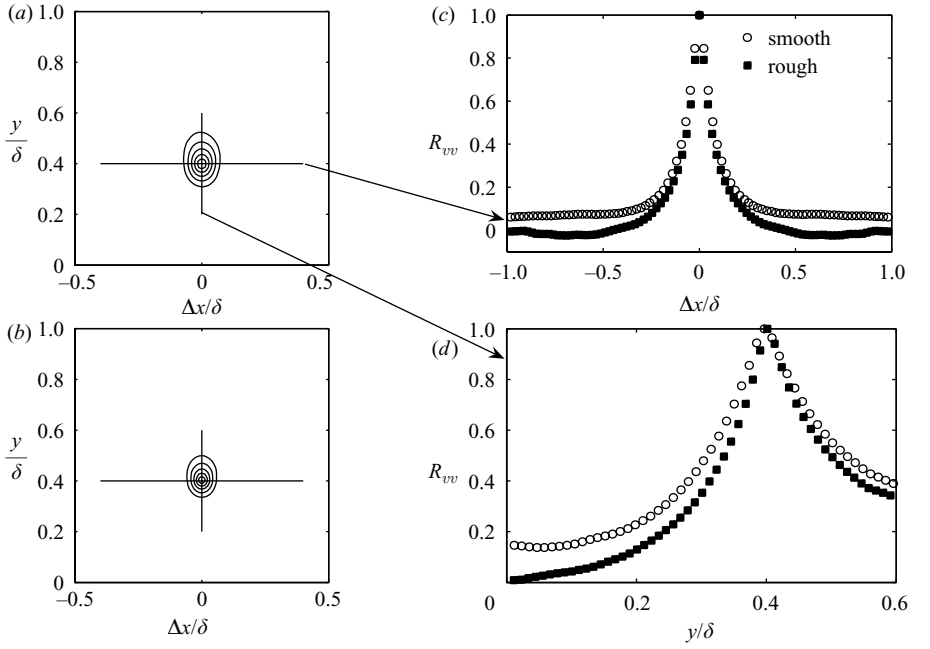


FIGURE 9. Contours of R_{vv} centred at $y/\delta = 0.4$, outermost contour $R_{vv} = 0.5$, contour spacing 0.1, (*a*) smooth wall, (*b*) rough wall, (*c*) streamwise slices through self-correlation points, (*d*) wall normal slices through self-correlation points.

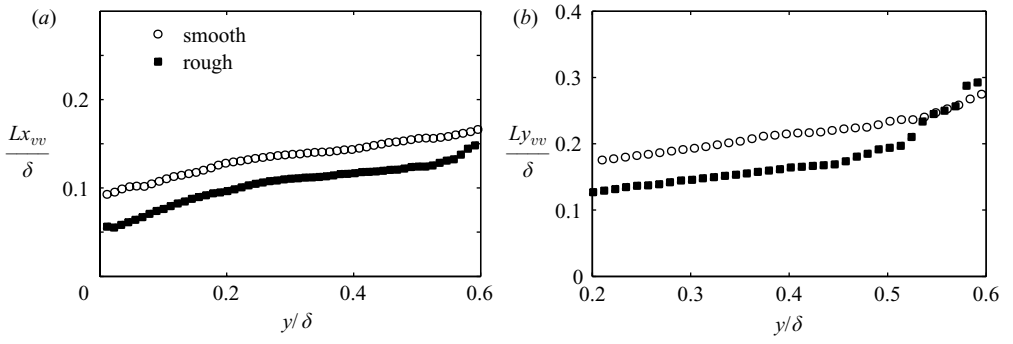


FIGURE 10. Extent of $R_{vv} = 0.5$ contour as a function of y/δ, (*a*) streamwise extent, (*b*) wall normal extent.

about 15 % lower than the smooth-wall correlation in both directions, but the cases otherwise appear similar.

Figure 14 shows contours of the cross-correlation of the signed swirl strength and streamwise velocity, $R_{\lambda u}$. Examples are shown with the correlation centred at $y/\delta = 0.15$ and 0.4 for the rough- and smooth-wall cases. Figure 15 shows the $R_{\lambda v}$ correlation for the same locations. Physically, $R_{\lambda u}$ and $R_{\lambda v}$ show the relation of a vortex centre to the surrounding velocity field. For example, consider a prograde (positive λ) swirling motion (e.g. the head of a hairpin vortex in the (x, y)-plane). In a reference frame moving with the vortex, there will be positively signed streamwise velocity above the vortex and negatively signed u below the vortex. The result will be positive and negative λu above and below the vortex, respectively. Similarly, prograde

https://doi.org/10.1017/S0022112007008518 Published online by Cambridge University Press

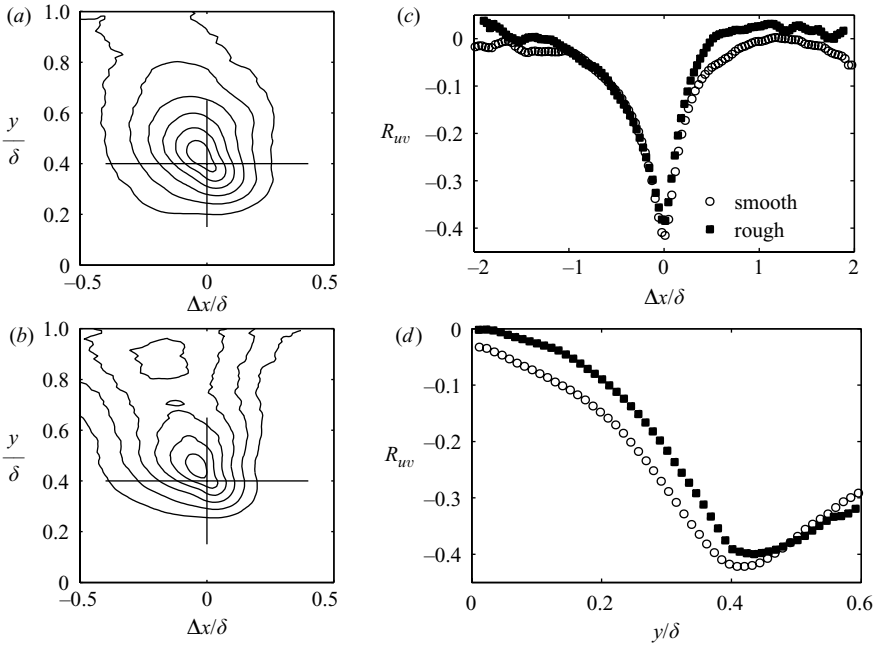


FIGURE 11. Contours of R_{uv} centred at $y/\delta = 0.4$, outermost contour $R_{uv} = -0.15$, contour spacing -0.05, (*a*) smooth wall, (*b*) rough wall, (*c*) streamwise slices through self-correlation points, (*d*) wall normal slices through self-correlation points.

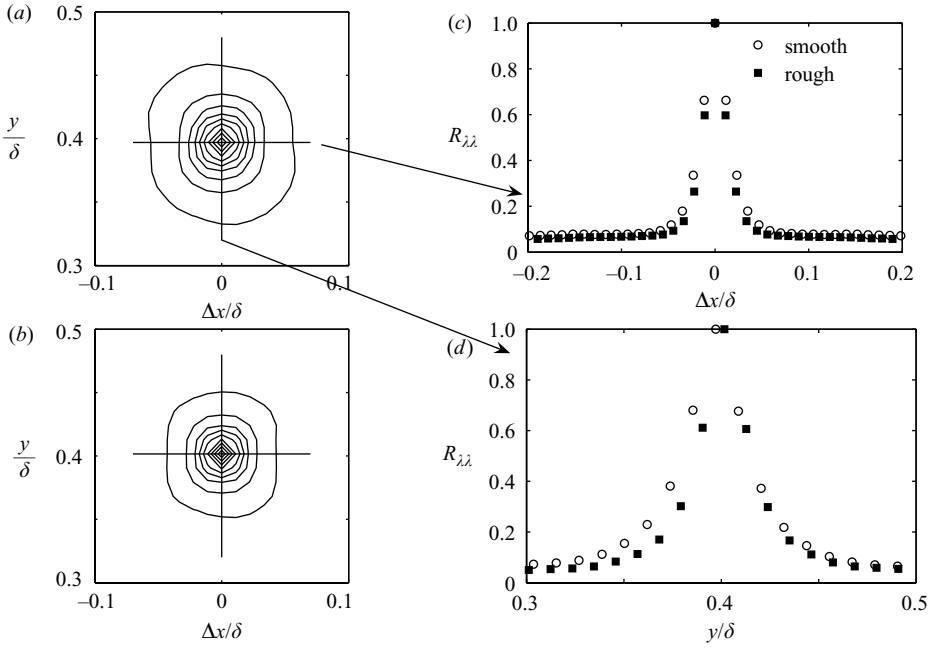


FIGURE 12. Contours of $R_{\lambda\lambda}$ centred at $y/\delta = 0.4$, outermost contour $R_{uv} = 0.1$, contour spacing 0.1, (*a*) smooth wall, (*b*) rough wall, (*c*) streamwise slices through self-correlation points, (*d*) wall normal slices through self-correlation points.

https://doi.org/10.1017/S0022112007008518 Published online by Cambridge University Press

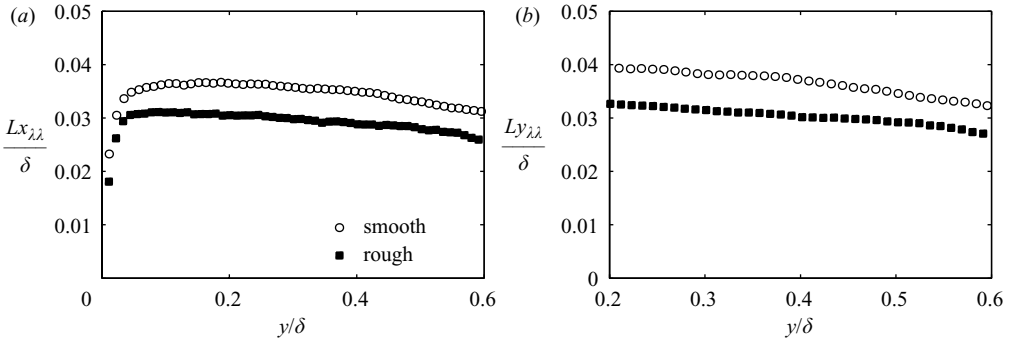


FIGURE 13. Extent of the $R_{\lambda\lambda} = 0.5$ contour as a function of y/δ, (*a*) streamwise extent, (*b*) wall normal extent.

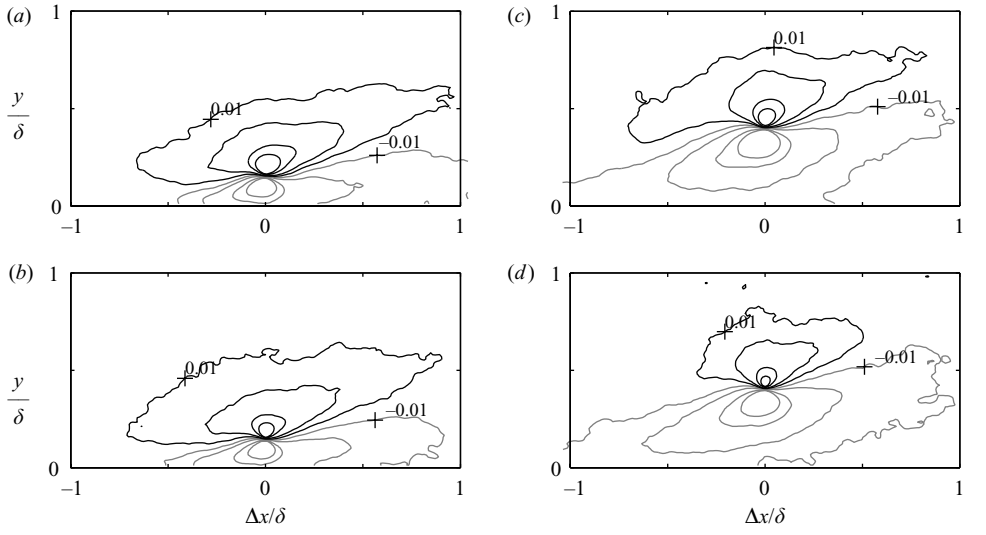


FIGURE 14. Contours of $R_{\lambda u}$ centred at $y/\delta = 0.4$, contour magnitudes $R_{\lambda u} = 0.01$, 0.03, 0.07, 0.1, contour signs black, positive; grey, negative, (*a*) smooth wall, $y/\delta = 0.15$, (*b*) rough wall, $y/\delta = 0.15$, (*c*) smooth wall, $y/\delta = 0.4$, (*d*) rough wall, $y/\delta = 0.4$.

rotation of the vortex means velocity toward the wall (negative v) downstream of the vortex centre and velocity away from the wall (positive v) upstream of the vortex. The resulting λv will be positive upstream and negative downstream of the vortex. The correlation coefficients show the average spatial extent and strength of the velocity field associated with a vortex centred at the self correlation point. If the vortex is part of a hairpin packet, the relation between the vortices in the packet and their associated velocity fields will extend the λu correlation along the length of the packet, as seen in figure 14. For both $R_{\lambda u}$ and $R_{\lambda v}$, the rough- and smooth-wall results are similar, and this similarity holds at all wall normal locations. Straight-line fits between the positive and negative contours of the $R_{\lambda u}$ fields in figure 14 have slopes between 10° and 15°. These inclination angles are consistent with the angles extracted from the R_{uu} contours of figure 6. The present $R_{\lambda u}$ and $R_{\lambda v}$ results agree with those of Christensen & Adrian (2001) from a smooth-wall channel flow.

https://doi.org/10.1017/S0022112007008518 Published online by Cambridge University Press

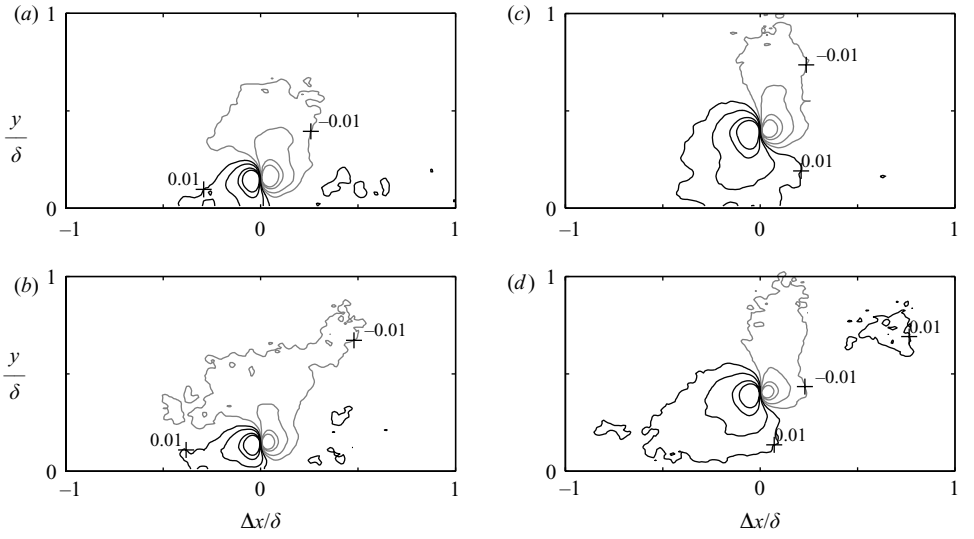


FIGURE 15. Contours of $R_{\lambda v}$ centred at $y/\delta = 0.4$, contour magnitudes $R_{\lambda v} = 0.01$, 0.03, 0.07, 0.1, contour signs black, positive; grey, negative, (*a*) smooth wall, $y/\delta = 0.15$, (*b*) rough wall, $y/\delta = 0.15$, (*c*) smooth wall, $y/\delta = 0.4$, (*d*) rough wall, $y/\delta = 0.4$.

Surface	Fraction non-zero swirl $y/\delta = 0.1$	$\overline{\lambda_m}\delta/u_\tau$ $y/\delta = 0.1$	Fraction non-zero swirl $y/\delta = 0.4$	$\overline{\lambda_m}\delta/u_\tau$ $y/\delta = 0.4$
Smooth Wall	0.0927	1.530	0.0879	1.103
Rough Wall	0.0921	1.571	0.0884	1.163

TABLE 2. Swirl strength in the (x, z)-plane.

3.3. *Velocity fields, (x, z)-plane*

Typical instantaneous velocity vector fields in the streamwise-spanwise plane at $y/\delta = 0.1$ and 0.4 are shown in figure 16. A Galilean decomposition has been applied at $y/\delta = 0.1$ with $0.72U_e$ and $0.56U_e$ subtracted from the streamwise velocity in the smooth- and rough-wall cases, respectively. At $y/\delta = 0.4$, $0.8U_e$ had been subtracted in both cases. The subtraction reveals high- and low-speed streaks. These streaks are more than an order of magnitude wider than the near-wall streaks of Kline *et al.* (1967). Contours of the signed swirl strength are superimposed on the vector fields. Swirl of opposite sign is located along each side of the low-speed regions. Tomkins & Adrian (2003) showed several examples of low-speed regions in the streamwise–spanwise plane flanked by lines of oppositely signed swirl. They explained that the low-speed streaks are induced by hairpin packets, and the vortices identified by the swirl strength correspond to the legs of hairpin vortices. The rough- and smooth-wall cases appear similar at both wall normal locations.

The fraction of the time the swirl strength is non-zero and the mean of the unsigned dimensionless swirl, $\overline{\lambda_m}\delta/u_\tau$, are given for the smooth and rough walls at both wall normal locations in table 2. The agreement between the smooth- and rough-wall cases at both locations is clear. The agreement is further illustrated by the probability density functions of $\lambda\delta/u_\tau$, shown in figure 17. The spikes at $\lambda\delta/u_\tau = 0$ are not

https://doi.org/10.1017/S0022112007008518 Published online by Cambridge University Press

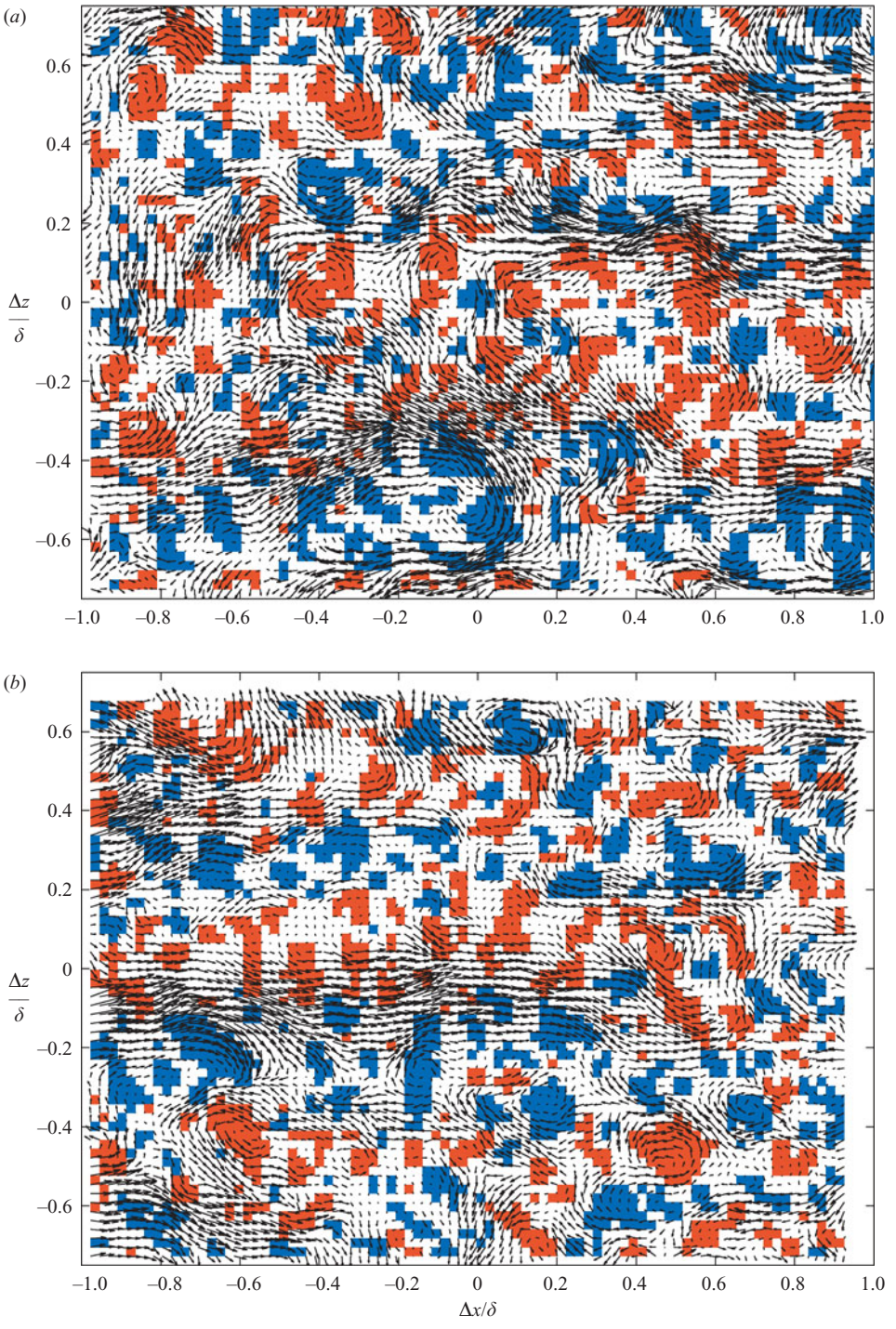


FIGURE 16(*a*, *b*). For caption see next page.

shown. As was shown for the swirl strength data in the (x, y)-plane (figure 5), the distributions in figure 17 agree with the probability density function distributions of gamma functions.

https://doi.org/10.1017/S0022112007008518 Published online by Cambridge University Press

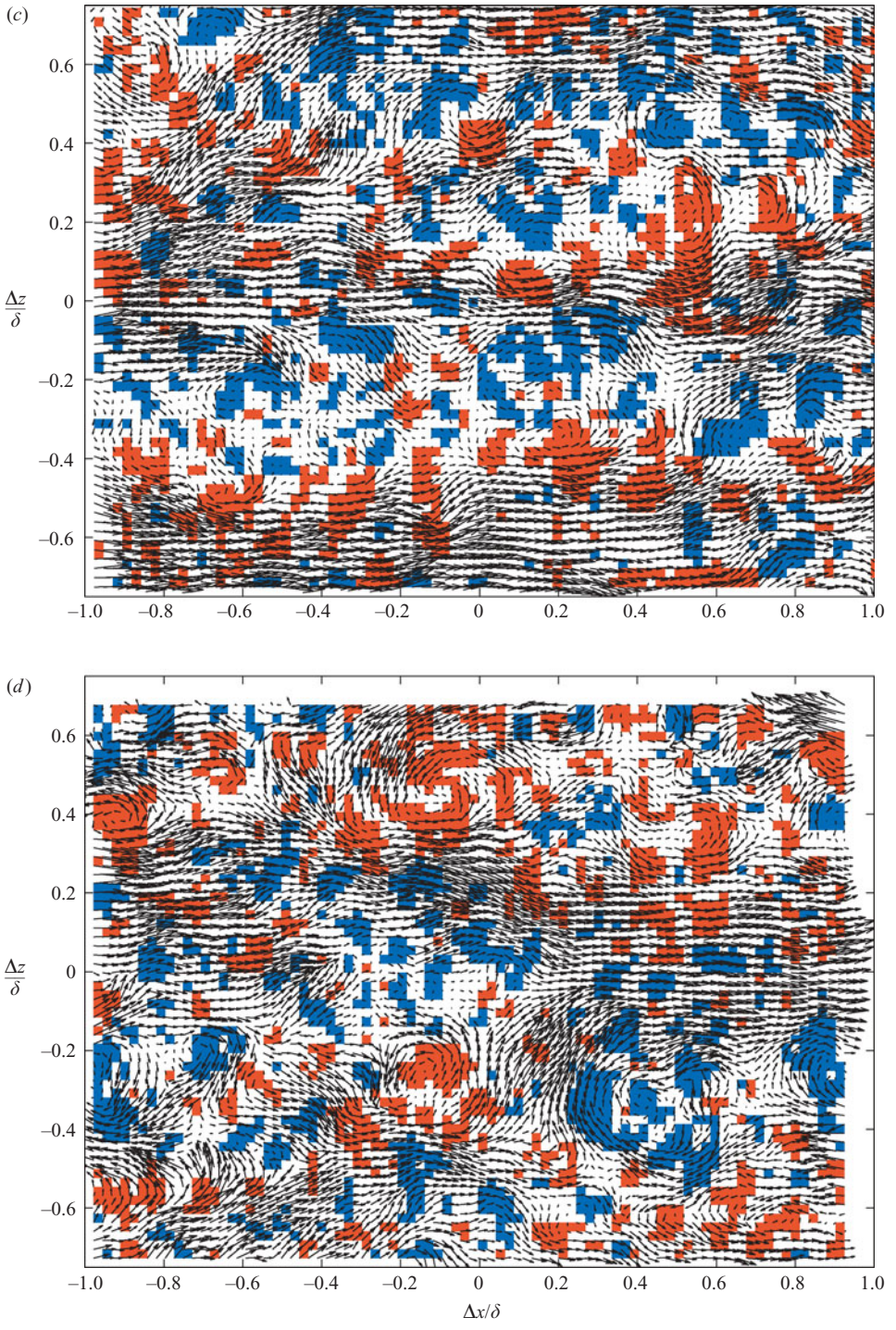


FIGURE 16. Typical instantaneous velocity field in the (x, z)-plane with positive swirl (red shading) and negative swirl (blue shading) superimposed, (a) smooth wall $y/\delta = 0.1$, (b) rough wall $y/\delta = 0.1$, (c) smooth wall $y/\delta = 0.4$, (d) rough wall $y/\delta = 0.4$.

https://doi.org/10.1017/S0022112007008518 Published online by Cambridge University Press

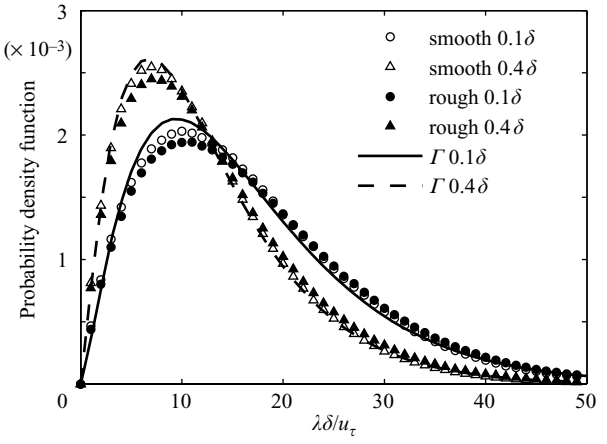


FIGURE 17. Probability density function of dimensionless swirl strength in the (x, z)-plane with Γ function p.d.f. fits to smooth-wall data.

Contours of the two-point correlation, R_{uu}, are shown in figure 18 for the rough- and smooth-wall cases at $y/\delta = 0.1$ and 0.4. Also shown are streamwise and spanwise slices through the self-correlation points. The high peak centred at the self-correlation point is similar for the rough- and smooth-wall cases. The extent of the high peak in the streamwise and spanwise directions is slightly larger at $y/\delta = 0.4$ than at $y/\delta = 0.1$. The values of the streamwise length, Lx_{uu}, at $y/\delta = 0.1$ and 0.4 obtained in the (x, z)-plane are in good agreement with the values obtained in the (x, y)-plane. Secondary correlation peaks of both positive and negative value are present as streamwise oriented streaks at various spanwise spacings from the self-correlation point. These streaks indicate a regular spacing of high- and low-speed regions. The correlation values are low compared to the central peak because there is variation in the streak spacing at any instant, as suggested by the vector fields in figure 16. From the contours of figure 18, the spacing between streaks of the same sign is about 0.75δ for the smooth wall at both y/δ locations, and about 0.85δ for the rough wall. The extent of the primary peak in the streamwise (Lx_{uu}) and spanwise (Lz_{uu}) directions is slightly larger for the smooth wall than for the rough, particularly at low values of R_{uu}, but the differences are typically less than 10 %. The present Lx_{uu} and Lz_{uu} results are about 20 % higher, but generally comparable to the smooth-wall results presented by Ganapathisubramani *et al.* (2005) and Hutchins *et al.* (2005). The present differences between the rough- and smooth-wall cases are comparable to the variation in these quantities among the smooth-wall cases of Hutchins *et al.* (2005).

Contours of R_{ww} are shown in figure 19 along with streamwise and spanwise slices through the self-correlation points. The rough- and smooth-wall results are similar. The streamwise extent of the correlation is much lower for R_{ww} than for R_{uu}. This is not surprising since the streamwise velocity is associated with the convection speed of the hairpin packets, whereas the spanwise velocity is not. Small differences are visible between the two wall normal locations. At both locations, the smooth- and rough-wall results are virtually identical. The present results are in good agreement with the smooth-wall results of Hutchins *et al.* (2005).

The cross-correlation R_{uw} is shown in figure 20. Similarity is clear between the smooth- and rough-wall results. The shape and signs of the contours are consistent with flow induced by the legs of hairpin vortices to the sides of the low-speed regions.

https://doi.org/10.1017/S0022112007008518 Published online by Cambridge University Press

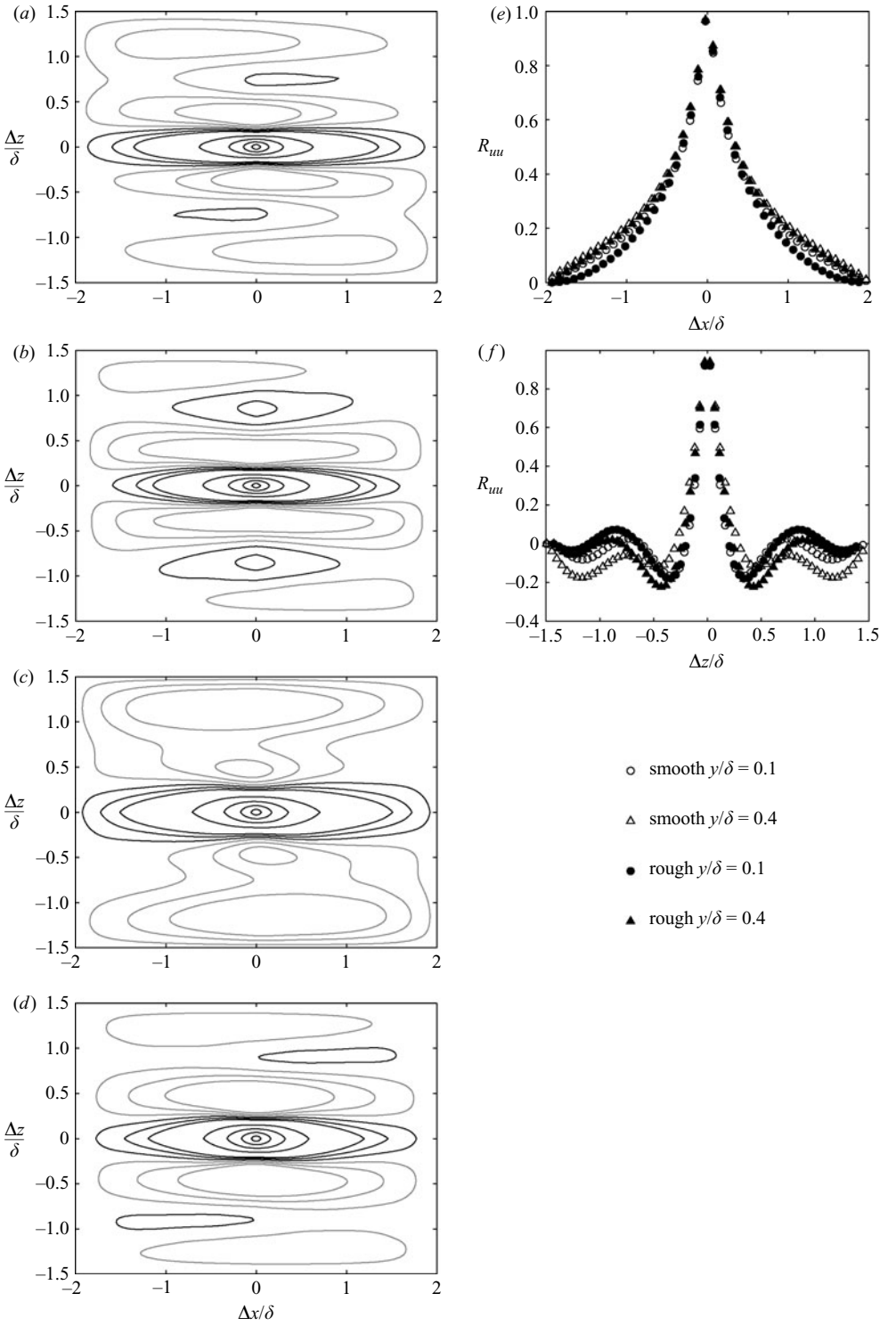


FIGURE 18. Contours of R_{uu} in the (x, z)-plane, contour magnitudes $R_{uu} = 0.02$, 0.06, 0.1, 0.3, 0.5, 0.7, 0.9, contour signs black, positive; grey, negative, (*a*) smooth wall $y/\delta = 0.1$, (*b*) rough wall $y/\delta = 0.1$, (*c*) smooth wall $y/\delta = 0.4$, (*d*) rough wall $y/\delta = 0.4$, (*e*) streamwise slices through self-correlation points, (*f*) spanwise slices through self-correlation points.

https://doi.org/10.1017/S0022112007008518 Published online by Cambridge University Press

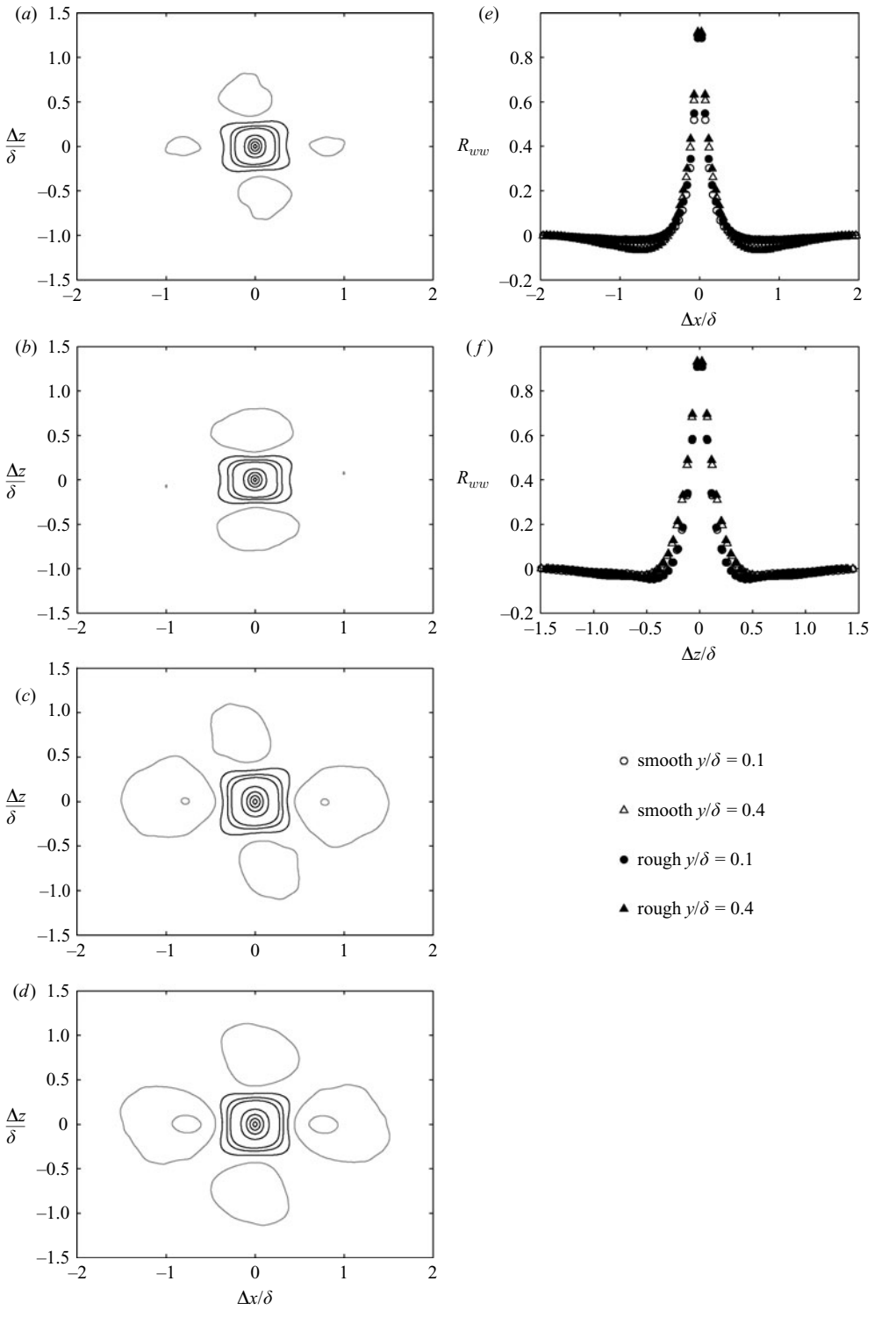


FIGURE 19. Contours of R_{ww} in the (x, z)-plane, contour magnitudes $R_{ww} = 0.02$, 0.06, 0.1, 0.3, 0.5, 0.7, 0.9, contour signs black, positive; grey, negative, (*a*) smooth wall $y/\delta = 0.1$, (*b*) rough wall $y/\delta = 0.1$, (*c*) smooth wall $y/\delta = 0.4$, (*d*) rough wall $y/\delta = 0.4$, (*e*) streamwise slices through self-correlation points, (*f*) spanwise slices through self-correlation points.

https://doi.org/10.1017/S0022112007008518 Published online by Cambridge University Press

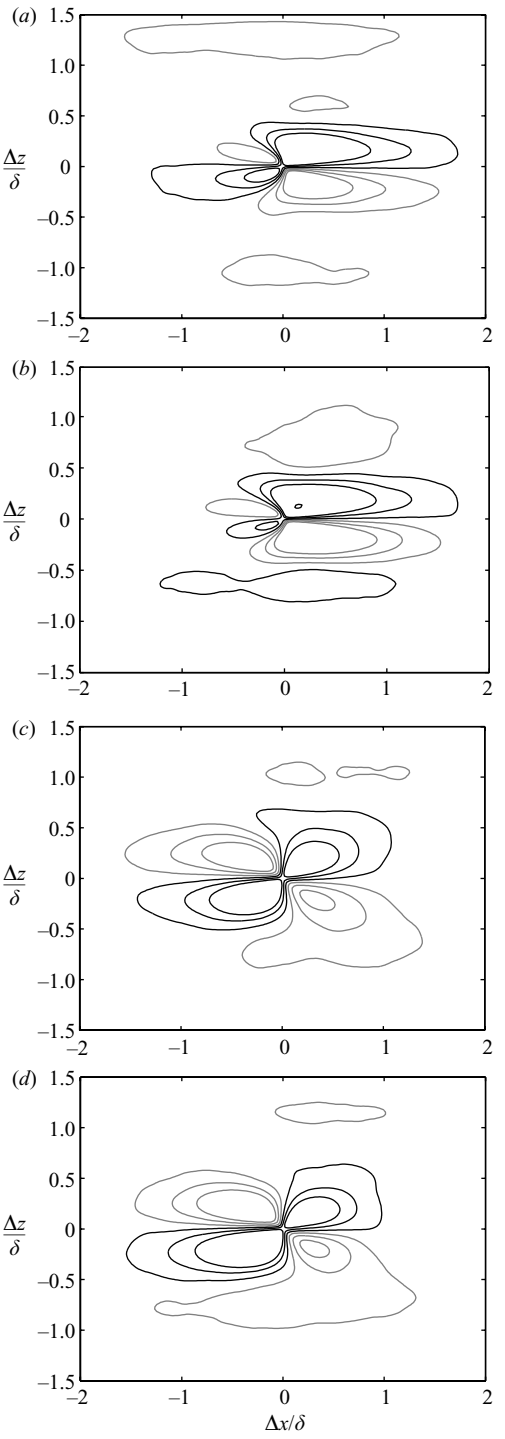


FIGURE 20. Contours of R_{uw} in the (x, z)-plane, contour magnitudes $R_{uw} = 0.02$, 0.06, 0.1, contour signs black, positive; grey, negative, (*a*) smooth wall $y/\delta = 0.1$, (*b*) rough wall $y/\delta = 0.1$, (*c*) smooth wall $y/\delta = 0.4$, (*d*) rough wall $y/\delta = 0.4$.

https://doi.org/10.1017/S0022112007008518 Published online by Cambridge University Press

The vortices direct fluid downstream (with $-u$) toward the self-correlation point from both spanwise sides (with oppositely signed w on either side). The fluid continues past the self-correlation point (still $-u$) and moves away from the self-correlation point in the spanwise direction (w changes sign on each side of the span). The contour shape is noticeably different between the $y/\delta = 0.1$ and 0.4 locations, and this difference is the same for the smooth- and rough-wall cases. The contours at $y/\delta = 0.1$ extend mainly downstream of the self-correlation point, while those at $y/\delta = 0.4$ extend both upstream and downstream. The difference may be due to a higher inclination angle of the vortices farther from the wall, as noted by Ganapathisubramani *et al.* (2006).

Two-point correlations of the signed swirl strength, $R_{\lambda\lambda}$, in the (x, z)-plane are shown in figure 21 along with streamwise and spanwise slices through the self-correlation points. The value of $R_{\lambda\lambda}$ drops off quickly from the self-correlation point. The rough- and smooth-wall cases are in good agreement. The present results are in good agreement with the smooth-wall results of Ganapathisubramani *et al.* (2006). In their results, Ganapathisubramani *et al.* (2006) noted that at the higher levels of $R_{\lambda\lambda}$, the extent of the correlation was the same at $y/\delta = 0.09$ and 0.53. For $R_{\lambda\lambda} < 0.1$, they saw that the streamwise extent of the correlation, $Lx_{\lambda\lambda}$, was larger than the spanwise extent $Lz_{\lambda\lambda}$, and they attributed this to streamwise elongation of large structures. They noted that the ratio $Lx_{\lambda\lambda}/Lz_{\lambda\lambda}$ was higher near the wall, which they attributed to eddies whose inclination angle increased with distance from the wall. The eddies are presumably the legs of hairpin vortices. Although the differences in $R_{\lambda\lambda}$ between $y/\delta = 0.1$ and 0.4 in the present results are subtle, they agree with the results of Ganapathisubramani *et al.* (2006). The very low-magnitude contours in figure 21 show streamwise streaks of correlated swirl. The sign of $R_{\lambda\lambda}$ in each streak alternates across the span. The spacing of the streaks is consistent with the R_{uu} result of figure 18. The agreement of $R_{\lambda\lambda}$ and R_{uu} is not coincidental. The low-speed regions are the result of hairpin packets, and the legs of the hairpins are aligned along the sides of the low-speed regions, as shown in figure 16. Tomkins & Adrian (2003) noted that the degree of coherence of the structures is remarkable given the background turbulence level, and it is also remarkable that the low-magnitude $R_{\lambda\lambda}$ contours can be extracted from the turbulent flow field to show correlation across multiple regions across the span.

The correlation between the signed swirl strength and the velocity field is shown in the $R_{\lambda u}$ contours of figure 22 along with spanwise slices through the self-correlation points. There is little variation between the rough- and smooth-wall cases. There is strong correlation of opposite sign to each side of the self-correlation point, indicating the relation of the hairpin legs to the low-speed regions. The maximum correlation is somewhat higher closer to the wall than at $y/\delta = 0.4$. The peak is somewhat wider in the spanwise direction at $y/\delta = 0.4$, possibly indicating larger structures farther from the wall. Streaks of lower $R_{\lambda u}$ indicate the regular spacing of the low-speed regions across the span. The spacing is the same for the rough- and smooth-wall cases, as indicated previously by the R_{uu} and $R_{\lambda\lambda}$ results.

Contours of $R_{\lambda w}$ are shown in figure 23 along with streamwise slices through the self-correlation points. The high-magnitude peaks correspond to vortices inducing spanwise motion at the self-correlation point. Lower magnitude contours indicate a correlation across the span, as seen more clearly above in R_{uu} and $R_{\lambda\lambda}$. The $R_{\lambda w}$ contours are clearly different at $y/\delta = 0.1$ and 0.4, suggesting a difference in the turbulence structure between the two locations. As in the R_{uw} contours of figure 20, the correlation is stronger downstream of the self-correlation point at $y/\delta = 0.1$, but

https://doi.org/10.1017/S0022112007008518 Published online by Cambridge University Press

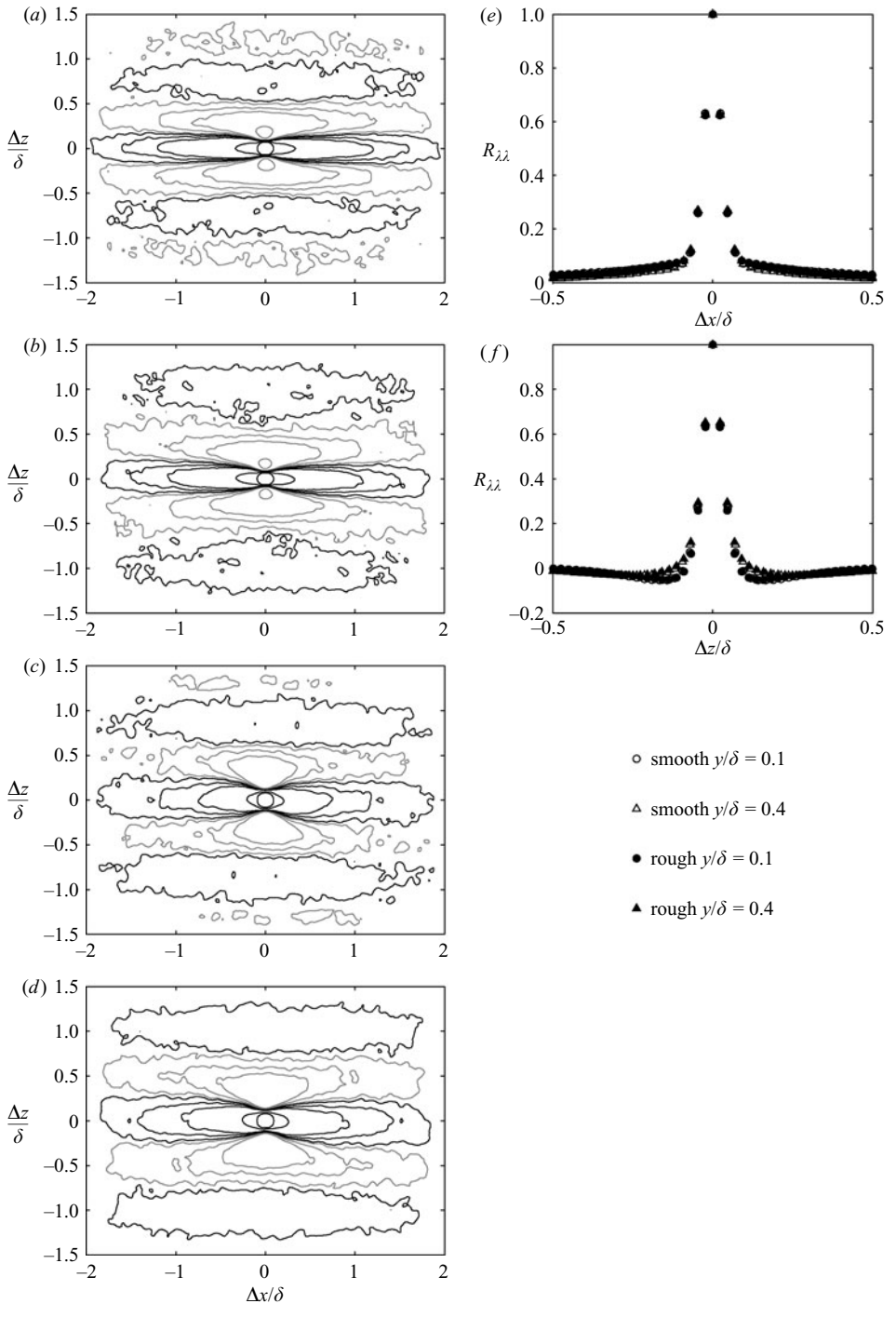


FIGURE 21. Contours of $R_{\lambda\lambda}$ in the (x, z)-plane, contour magnitudes $R_{\lambda\lambda} = 0.001$, 0.005, 0.01, 0.04, 0.08, contour signs black, positive; grey, negative, (*a*) smooth wall $y/\delta = 0.1$, (*b*) rough wall $y/\delta = 0.1$, (*c*) smooth wall $y/\delta = 0.4$, (*d*) rough wall $y/\delta = 0.4$, (*e*) streamwise slices through self-correlation points, (*f*) spanwise slices through self-correlation points.

https://doi.org/10.1017/S0022112007008518 Published online by Cambridge University Press

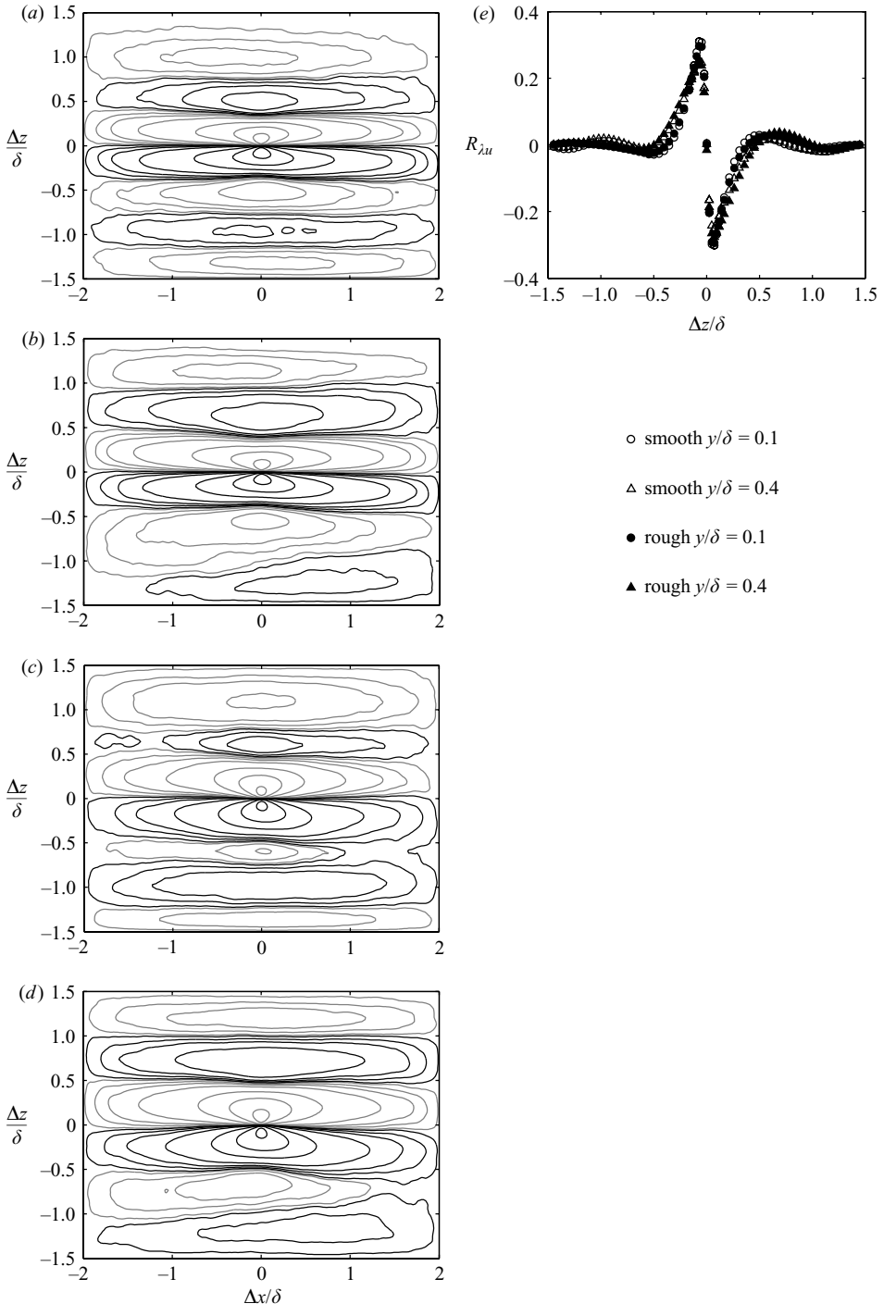


FIGURE 22. Contours of $R_{\lambda u}$ in the (x, z)-plane, contour magnitudes $R_{\lambda u} = 0.001$, 0.005, 0.01, 0.02, 0.05, 0.1, 0.2, contour signs black, positive; grey, negative, (*a*) smooth wall $y/\delta = 0.1$, (*b*) rough wall $y/\delta = 0.1$, (*c*) smooth wall $y/\delta = 0.4$, (*d*) rough wall $y/\delta = 0.4$, (*e*) spanwise slices through self correlation points.

https://doi.org/10.1017/S0022112007008518 Published online by Cambridge University Press

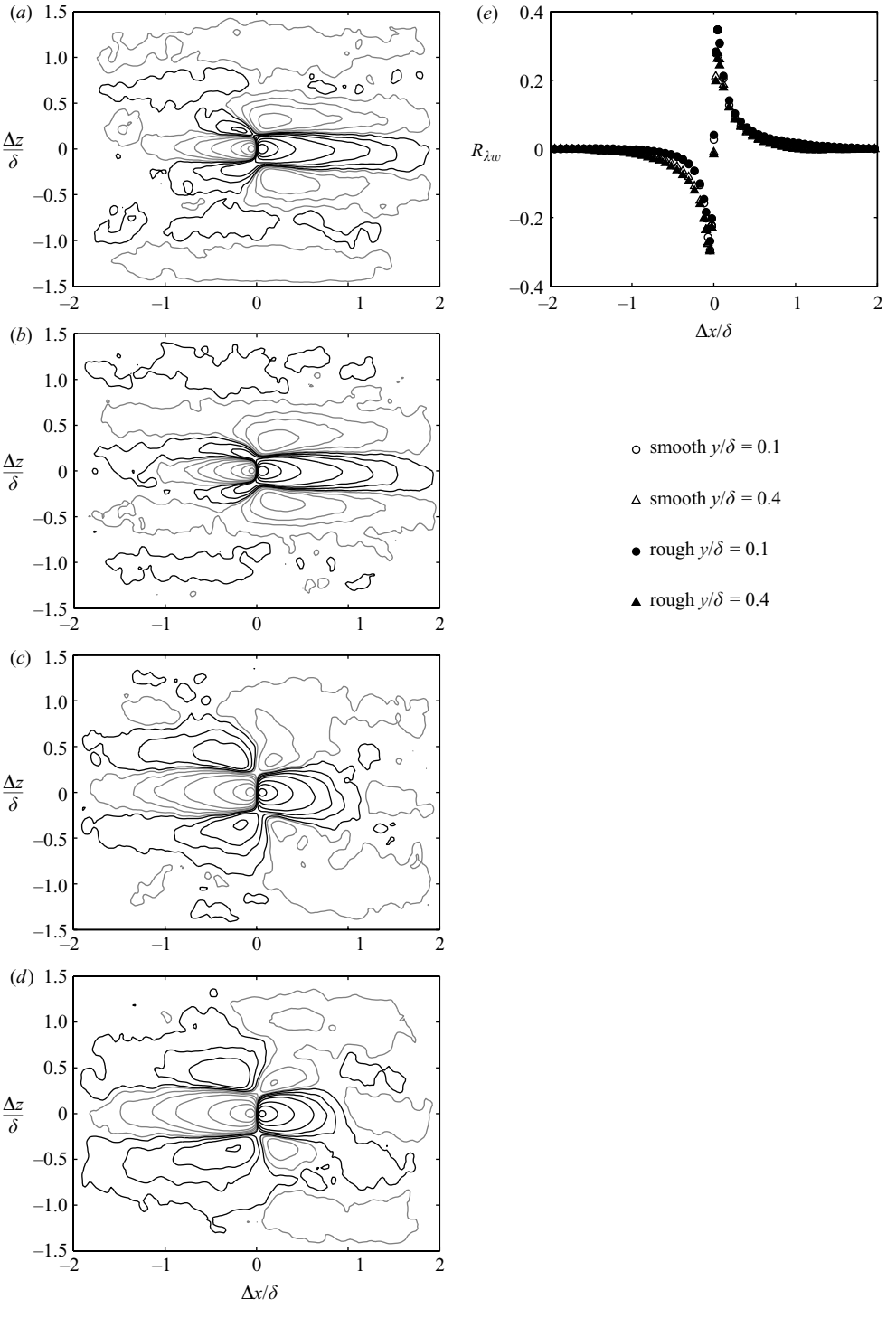


FIGURE 23. Contours of $R_{\lambda w}$ in the (x, z)-plane, contour magnitudes $R_{\lambda w} = 0.001$, 0.005, 0.01, 0.02, 0.05, 0.1, 0.2, contour signs black, positive; grey, negative, (*a*) smooth wall $y/\delta = 0.1$, (*b*) rough wall $y/\delta = 0.1$, (*c*) smooth wall $y/\delta = 0.4$, (*d*) rough wall $y/\delta = 0.4$, (*e*) streamwise slices through self-correlation points.

https://doi.org/10.1017/S0022112007008518 Published online by Cambridge University Press

stronger upstream at $y/\delta = 0.4$. At both locations, the similarity of the magnitude and details of the contour patterns between the smooth- and rough-wall results is clear.

4. Conclusions

Experimental measurements have been presented from smooth- and rough-wall boundary layers to document the turbulence structure under zero-pressure-gradient conditions. On the smooth wall, the focus was on a streamwise location where the momentum-thickness Reynolds number was high (6069). On the rough wall, the focus was on a streamwise location where the momentum-thickness Reynolds number (7663) was close to that of the smooth-wall case. Fully rough conditions were established using k-type roughness produced with a wire mesh ($k_s^+ = 112$). Measurements were made in the streamwise–wall normal plane, and in two streamwise–spanwise planes located at $y/\delta = 0.1$ and 0.4. Turbulence structure was documented through spectra of the streamwise and wall normal fluctuating velocity, the swirl strength in each measurement plane, and two-point auto- and cross-correlations of the velocity components and swirl strength.

The present results all show excellent qualitative agreement between the turbulence structure in the outer region for rough- and smooth-wall boundary layers, supporting Townsend's (1976) Reynolds-number-similarity hypothesis. Hairpin packets are observed to be a prominent feature of the rough-wall boundary layer, much the same as its smooth-wall counterpart. Some quantitative differences were noted between the smooth- and rough-wall results, mainly observed as differences in the correlation lengths. The lengths based on R_{vv}, R_{uv} and $R_{\lambda\lambda}$ are about 10 to 20 % lower on the rough wall. Other quantities showed closer agreement. The turbulence spectra, normalized swirl strength, two-point correlations of various quantities, and average angles of maximum correlation all show very good quantitative agreement. These results indicate that the outer layer is largely independent of surface condition except for the role that the wall conditions have on setting the length (δ) and velocity (u_τ) boundary conditions for the outer flow. The present results support the previously reported similarity in outer-region turbulence statistics between smooth- and rough-wall boundary layers.

The present results agree with the body of literature documenting turbulence structure in smooth-wall boundary layers. The boundary layer includes large-scale packets consisting of multiple hairpin vortices. The packets have a characteristic inclination angle and size which scales on the boundary-layer thickness, and these quantities are consistent between the rough- and smooth-wall cases.

The authors would like to thank the Office of Naval Research for providing financial support under Grants N00014-06-WR-2-0069 and N00014-06-WR-2-0218 and the United States Naval Academy Hydromechanics Laboratory for providing technical support.

REFERENCES

Adrian, R. J. 1983 Laser velocimetry. In *Fluid Mechanics Measurements* (ed. R. J. Goldstein) Hemisphere.

Adrian, R. J., Christensen, K. T. & Liu, Z.-C. 2000*a* Analysis and interpretation of instantaneous turbulent velocity fields. *Exps. Fluids* **29**, 275–290.

Adrian, R. J., Meinhart, C. D. & Tomkins, C. D. 2000*b* Vortex organization in the outer region of the turbulent boundary layer. *J. Fluid Mech.* **422**, 1–54.

https://doi.org/10.1017/S0022112007008518 Published online by Cambridge University Press

Antonia, R. A., Bisset, D. K. & Browne, L. W. B. 1990 Effect of Reynolds number on the topology of the organized motion in a turbulent boundary layer. *J. Fluid Mech.* **213**, 267–286.

del Álamo, J. C. & Jiménez, J. 2003 Spectra of the very large anisotropic scales in turbulent channels. *Phys. Fluids* **15**, L41–L44.

Bhaganagar, K., Kim, J. & Coleman, G. 2004 Effect of roughness on wall-bounded turbulence. *Flow Turb. Combust.* **72**, 463–492.

Chong, M. S., Perry, A. E. & Cantwell, B. J. 1990 A general classification of three-dimensional flow fields. *Phys. Fluids* A **2**, 765–777.

Christensen, K. T. & Adrian, R. J. 2001 Statistical evidence of hairpin vortex packets in wall turbulence. *J. Fluid Mech.* **431**, 433–443.

Christensen, K. T. & Wu, Y. 2005 Characteristics of vortex organization in the outer layer of wall turbulence. *Proc. Fourth Intl Symp. on Turbulence and Shear Flow Phenomena, Williamsburg, Virginia*, vol. 3, pp. 1025–1030.

Flack, K. A., Schultz, M. P. & Shapiro, T. A. 2005 Experimental support for Townsend's Reynolds number similarity hypothesis on rough walls. *Phys. Fluids* **17**, #035102.

Flack, K. A., Schultz, M. P. & Connelly, J. S. 2007 Examination of a critical roughness height for boundary layer similarity. *Phys. Fluids* **19**, 095104.

Ganapathisubramani, B., Longmire, E. K. & Marušić, I. 2003 Characteristics of vortex packets in turbulent boundary layers. *J. Fluid Mech.* **478**, 35–46.

Ganapathisubramani, B., Hutchins, N., Longmire, E. K. & Marušić, I. 2005 Investigation of large-scale coherence in a turbulent boundary layer using two-point correlations. *J. Fluid Mech.* **524**, 57–80.

Ganapathisubramani, B., Longmire, E. K. & Marušić, I. 2006 Experimental investigation of vortex properties in a turbulent boundary layer. *Phys. Fluids* **18**, #055105.

Grass, A. J. 1971 Structural features of turbulent flow over smooth and rough boundaries. *J. Fluid Mech.* **50**, 233–255.

Guala, M., Hommema, S. E. & Adrian, R. J. 2006 Large-scale and very-large-scale motions in turbulent pipe flow. *J. Fluid Mech.* **554**, 521–542.

Hambleton, W. T., Hutchins, N. & Marušić, I. 2006 Simultaneous orthogonal-plane particle image velocimetry measurements in a turbulent boundary layer. *J. Fluid Mech.* **560**, 53–64.

Head, M. R. & Bandyopadhyay, P. 1981 New aspects of turbulent boundary-layer structure. *J. Fluid Mech.* **107**, 297–337.

Hutchins, N., Hambleton, W. T. & Marušić, I. 2005 Inclined cross-stream stereo particle image velocimetry measurements in turbulent boundary layers. *J. Fluid Mech.* **541**, 21–54.

Jiménez, J. 2004 Turbulent flows over rough walls. *Annu. Rev. Fluid Mech.* **36**, 173–196.

Keirsbulck, L., Labraga, L., Mazouz, A. & Tournier, C. 2002 Surface roughness effects on turbulent boundary layer structures. *Trans. ASME* I: *J. Fluids Engng* **124**, 127–135.

Kline, S. J., Reynolds, W. C., Schraub, F. A. & Rundstadler, P. W. 1967 The structure of turbulent boundary layers. *J. Fluid Mech.* **30**, 741–773.

Krogstad, P.-Å. & Antonia, R. A. 1994 Structure of turbulent boundary layers on smooth and rough walls. *J. Fluid Mech.* **277**, 1–21.

Krogstad, P.-Å., Antonia, R. A. & Browne, L. W. B. 1992 Comparison between rough- and smooth-wall turbulent boundary layers. *J. Fluid Mech.* **245**, 599–617.

Kunkel, G. J. & Marušić, I. 2006 Study of the near-wall-turbulent region of the high-Reynolds-number boundary layer using an atmospheric flow. *J. Fluid Mech.* **548**, 375–402.

Leonardi, S., Orlandi, P., Smalley, R. J., Djenidi, L. & Antonia, R. A. 2003 Direct numerical simulations of turbulent channel flow with transverse square bars on one wall. *J. Fluid Mech.* **491**, 229–238.

Marušić, I. 2001 On the role of large-scale structures in wall turbulence. *Phys. Fluids* **13**, 735–743.

Na, Y., Hanratty, T. J. & Liu, Z. 2001 The use of DNS to define stress producing events for turbulent flow over a smooth wall. *Flow Turb. Combust.* **66**, 495–512.

Nakagawa, S. & Hanratty, T. J. 2001 Particle image velocimetry measurements of flow over a wavy wall. *Phys. Fluids* **13**, 3504–3507.

Perry, A. E. & Chong, M. S. 1982 On the mechanism of wall turbulence. *J. Fluid Mech.* **119**, 173–217.

Perry, A. E. & Marušić, I. 1995 A wall-wake model for the turbulence structure of boundary layers. Part 1. Extension of the attached eddy hypothesis. *J. Fluid Mech.* **298**, 361–388.

https://doi.org/10.1017/S0022112007008518 Published online by Cambridge University Press

Raupach, M. R., Antonia, R. A. & Rajagopalan, S. 1991 Rough-wall boundary layers. *Appl. Mech. Rev.* **44**, 1–25.

Schultz, M. P. & Flack, K. A. 2007 The rough-wall turbulent boundary layer from the hydraulically smooth to the fully rough regime. *J. Fluid Mech.* **580**, 381–405.

Shockling, M. A., Allen, J. J. & Smits, A. J. 2006 Roughness effects in turbulent pipe flow. *J. Fluid Mech.* **564**, 267–285.

Tachie, M. F., Bergstrom, D. J. & Balachandar, R. 2000 Rough wall turbulent boundary layers in shallow open channel flow. *Trans. ASME* I: *J. Fluids Engng* **122**, 533–541.

Theodorson, T. 1952 Mechanism of turbulence. *Proc. Second Midwestern Conf. on Fluid Mechanics*, Ohio State University, Columbus, Ohio.

Tomkins, C. D. & Adrian, R. J. 2003 Spanwise structure and scale growth in turbulent boundary layers. *J. Fluid Mech.* **490**, 37–74.

Townsend, A. A. 1976 *The Structure of Turbulent Shear Flow*, 2nd edn. Cambridge University Press.

Wei, T. & Willmarth, W. W. 1989 Reynolds-number effects on the structure of a turbulent channel flow. *J. Fluid Mech.* **204**, 57–95.

Wu, Y. & Christensen, K. T. 2006 Population trends of spanwise vortices in wall turbulence. *J. Fluid Mech.* **568**, 55–76.

Zhou, J., Adrian, R. J., Balachandar, S. & Kendall, T. M. 1999 Mechanisms for generating coherent packets of hairpin vortices in channel flow. *J. Fluid Mech.* **387**, 353–396.

https://doi.org/10.1017/S0022112007008518 Published online by Cambridge University Press